



Lunar cryptomaria: Mineralogy and composition of ancient volcanic deposits

Jennifer Whitten ^{a,*}, James W. Head ^b

^a Smithsonian Institution, Center for Earth and Planetary Studies, MRC 315, PO Box 37012, Washington, DC 20013-7012, USA

^b Department of Earth, Environmental and Planetary Sciences, Brown University, Providence, RI 02912, USA



ARTICLE INFO

Article history:

Received 17 June 2014

Received in revised form

23 October 2014

Accepted 27 November 2014

Available online 6 December 2014

Keywords:

Moon

Volcanism

Cryptomaria

Moon Mineralogy Mapper

Visible to near infrared

Spectroscopy

Modified Gaussian Model (MGM)

ABSTRACT

Ancient lunar volcanic deposits, known as cryptomaria, have been detected by remote telescopic and orbital measurements since the 1970s. Cryptomaria are most easily identified by the presence of dark-halo impact craters and are associated with a mare basalt mineralogy, which is indicated by two pyroxene spectral absorption features near 1 μm and 2 μm in the visible to near-infrared (VNIR) wavelengths. However, there are many early igneous lithologies that have been identified in the Apollo sample collection that have a similar VNIR spectral signal, implying a pyroxene-dominant mineralogy. In this study we use high resolution Moon Mineralogy Mapper (M^3) VNIR spectral data and the Modified Gaussian Model (MGM) to determine cryptomare mineralogy as well as Lunar Prospector gamma-ray spectrometer (LP GRS) FeO and Th compositional measurements to evaluate which ancient igneous rocks (e.g., low-Ti mare basalt, high-Ti mare basalt, Mg-suite rocks, dunite, high-Al mare basalt, KREEP basalt) are consistent with our mineralogical observations. In addition, spectra from different M^3 optical periods were compared to determine how the MGM-derived absorption band centers vary between datasets. Band center differences between optical periods are on the order of $\sim 6 \pm 4$ nm and $\sim 25 \pm 10$ nm for the 1 μm and 2 μm features, respectively. Cryptomare mineralogies are dominated by clinopyroxene and are consistent with measurements from locally exposed mare basalts. LP GRS measurements support a mare basalt rock type when regolith mixing is taken into account.

© 2014 Elsevier Ltd. All rights reserved.

1. Introduction and background

Ancient lunar volcanic deposits, known as cryptomaria (Head and Wilson, 1992), have been identified beneath basin ejecta deposits (e.g., Schultz and Spudis, 1979, 1983; Hawke and Spudis, 1980; Hawke and Bell, 1981; Bell and Hawke, 1984; Hawke et al., 1993, 2002, 2005, 2013; Head et al., 1993; Antonenko et al., 1995; Blewett et al., 1995; Mustard and Head, 1996; Antonenko, 1999; Giguere et al., 2003; Campbell and Hawke, 2005; Lawrence et al., 2008). The name assigned to these ancient volcanic deposits, cryptomaria, implies that these ancient volcanic deposits are mare basalts. However, mare basalts are not the only ancient igneous lithology that was produced on the Moon during its earliest geologic history. Samples returned from the Apollo missions indicate that a diverse suite of ancient rock types, including ferroan anorthosites, KREEP basalts, high-Al mare basalts, and Mg-suite rocks such as troctolites, dunites, norites, and gabbros (e.g., Warren and Wasson, 1977) formed during the final stages of the lunar magma ocean crystallization and shortly thereafter. The

primary lunar crust is dominated by ferroan anorthosites (Smith et al., 1970; Wood et al., 1970), while extrusive KREEP basalts and intrusive Mg-suite rocks are derived from melts of the lunar mantle (Warren and Wasson, 1977). The few dated samples of Mg-suite rocks and KREEP basalts indicate ancient ages > 3.8 Ga, immediately after the Imbrium formation event (Nyquist et al., 1975; Papanastassiou and Wasserburg, 1976; Ryder and Spudis, 1980; Nyquist and Shih, 1992; Stöffler et al., 2006). There is no indication that these lithologies continued to be produced after 3.8 Ga. The paucity of Mg-suite and KREEP basalt rocks in the sample collection could be due to a preservation effect, since much of the lunar nearside has been resurfaced by mare basalts over the last 3.8 Ga (Hiesinger et al., 2011), or it could be due to a cessation of their formation process. Whatever the cause of the paucity of the Mg-suite and KREEP basalts, mare basalts became the dominant igneous rock type for the remainder of the Moon's volcanic history.

Deconvolving the composition of ancient volcanic materials has important implications for the thermal history of the Moon. Analyses of mare basalt ages and their distribution provide information about mantle dynamics, including the timing of magma ocean overturn and the formation of mare basalt source regions in the mantle. Cryptomaria composition is also important

* Corresponding author. Tel.: +1 202 633 1585.

E-mail address: WhittenJ@si.edu (J. Whitten).

for determining the composition of magmas melting within and being erupted from the mantle. For instance, Mg-rich mantle melts may have been produced early in lunar history, intruding into the anorthositic crust, and it is only after mantle overturn (e.g., Hess and Parmentier, 1995) that the mare basalt source regions were established and able to melt. The frequency distribution of mare basalt crater retention ages (Hiesinger et al., 2011) shows a peak in the flux of volcanic activity around ~3.6 Ga. Returned samples tell the story of a much more compositionally and temporally diverse volcanic history compared to the mare basalt deposits. During the first ~500 My, the Moon was simultaneously producing mare basalts, KREEP basalts, and Mg-suite rocks (Ryder and Spudis, 1980; Taylor et al., 1983; Nyquist and Shih, 1992; Stöffler et al., 2006; Terada et al., 2007). Soon afterwards, around 3.8 Ga, there was either a substantial increase in the eruption of mare basalts or a decrease in the production of parental melts for KREEP basalts and Mg-suite rocks, or both processes occurred simultaneously.

Cryptomaria were first identified by the presence of dark-halo impact craters (DHCs) (Schultz and Spudis, 1979, 1983), which are small impact craters, <10 km in diameter, that excavate low albedo material from beneath higher-albedo surface material; these are not to be confused with other dark-halo craters interpreted as volcanic vents (e.g., Shoemaker, 1962; Head and Wilson, 1979). Initially, the DHC compositions were reported as basaltic, with some deposits being enriched in magnesium and KREEP (Schultz and Spudis, 1979). Geochemical analyses of cryptomaria utilized measurements of elemental ratios, such as Mg/Al and Mg/Si, and elemental abundances (thorium and iron) from gamma-ray and x-ray spectrometer data (Hawke and Spudis, 1980; Maxwell and Andre, 1981; Lawrence et al., 2008). Measurements of elemental abundances over regions of the lunar surface with a high concentration of DHCs were compared with mare basalts and KREEP-rich basalts in order to ascertain the composition of the buried volcanic material. These geochemical surface measurements of DHCs resulted in a variety of interpretations, including the presence of Mg-rich basalts, mare basalts, and KREEP-rich basalts (e.g., Schultz and Spudis, 1979; Hawke and Spudis, 1980; Lawrence et al., 2008).

Further geochemical and visible to near-infrared (VNIR) spectral analyses suggested that the compositions of DHCs were consistent with mare basalt material (Maxwell and Andre, 1981; Hawke and Spudis, 1980; Hawke and Bell, 1981; Bell and Hawke, 1984; Blewett et al., 1995; Giguere et al., 2003; Hawke et al., 2005; Lawrence et al., 2008). DHC VNIR spectral measurements are dominated by two pyroxene absorption features centered near 1 μm and 2 μm. At VNIR wavelengths, the center wavelength of the different absorption bands provides information about the composition of the pyroxene; longer wavelength 1 μm and 2 μm absorption features are associated with Fe- and Ca-rich pyroxenes (Adams, 1974; Cloutis and Gaffey, 1991) and are consistent with mare basalts. As a result of the systematic change in band center with mineral composition, many spectral studies of DHCs have focused on measuring the position of the pyroxene absorption band centers and comparing those values to the composition of known lunar samples (e.g., Bell and Hawke, 1984) or exposed mare basalt deposits from the same image scene (Blewett et al., 1995; Giguere et al., 2003; Hawke et al., 2005).

The mineralogy and composition of identified ancient volcanic deposits is important for understanding the early volcanic history of the Moon and the petrologic relationship between the different ancient igneous lithologies. Therefore, we have undertaken a study of the mineralogy of DHCs identified in Whitten and Head (2015) using Moon Mineralogy Mapper (M^3) VNIR spectral data, as well as an analysis of LP GRS elemental data. The purpose of this investigation is to: (1) determine the mineralogy of mapped cryptomaria to ascertain if some or all of the deposits are mare

basalts, (2) investigate the mineralogical variations both within a cryptomare region and also between cryptomare regions, (3) measure the compositional characteristics (Th and FeO) of all identified cryptomaria to further characterize and constrain their compositions, and (4) understand how calculated cryptomaria mineralogies compare with ancient volcanic lithologies from the Apollo sample collection. Despite the fact that the Mg-suite is interpreted as intrusive, the Mg-suite lithologies (e.g., troctolite, norite) are included in this analysis in order to make the fewest number of assumptions about the mineralogy and composition of cryptomaria; at some time during early lunar history conditions may have been such that the eruption of Mg-suite parental magmas was possible (Prissel et al., 2013).

2. Methods

2.1. Collection of VNIR spectra

All of the VNIR spectra used in this study were collected from the Moon Mineralogy Mapper (M^3) dataset (Boardman et al., 2011; Clark et al., 2011; Green et al., 2011; Besse et al., 2013). M^3 was a VNIR imaging spectrometer aboard the Chandrayaan-1 spacecraft that collected mineralogic information about the Moon's surface in 85 bands, from approximately 0.4–3.0 μm, at a spatial resolution of 140–280 m/pixel, depending on the spacecraft altitude (Pieters et al., 2009; Green et al., 2011). All spectra examined in this study were collected from M^3 mosaics composed of individual data strips (Table S3) and have a spatial resolution of 140 m/pixel. A total of 1020 reflectance spectra (3 × 3 pixel averages) were collected from individual DHCs located within 20 mapped cryptomare locations and any associated exposed mare basalt deposits (Figs. 1a and S1; Tables S1 and S2) (Whitten and Head, 2015). Each region of mapped cryptomare contains between 1 and 40 individual volcanic ponds (Fig. S1) and between one and three DHCs were sampled from each volcanic pond (Table S4). All DHC spectra within an individual volcanic pond were investigated and only those with the strongest absorptions were sampled for analysis. These individual DHC spectra were then averaged together to produce a single diagnostic spectrum for each volcanic pond within a given cryptomare region. The 1020 individual cryptomare and mare spectra were thus reduced to a total of 414 diagnostic spectra; each cryptomare region has multiple spectral measurements, one for each individual volcanic pond (Tables S1, S2 and S4).

A ground truth correction derived from laboratory spectra of feldspathic lunar soils was applied to the sampled M^3 spectra. This correction improves the accuracy of the position of the M^3 1 μm absorption feature and is especially relevant for spectral analyses involving highland soils (Isaacson et al., 2013). The spectral data used in this study were collected from multiple M^3 optical periods, including 1b, 2c1, and 2c2. The shape of spectra collected during different M^3 optical periods varies depending on the detector temperature; spectra collected during "hot" optical periods where temperatures exceeded ~160 K (2c1 and May 20–July 9, 2009 of 2c2) required a different ground truth correction (Isaacson et al., 2013) compared with spectral data from "cold" optical periods (1b and July 12–August 16, 2009 of 2c2) (Green et al., 2011). In order to quantify the spectral differences between optical periods, we compared the Modified Gaussian Model (MGM)-derived 1 μm and 2 μm absorption band centers from the same sample location in two different optical periods. Austral, Dewar, Langemak, Lomonosov–Fleming and Van de Graaff spectra were used for the optical period 2c2–2c1 comparisons while spectra from Cleomedes, Frigoris, Mendel–Rydberg, Schiller–Schickard, Taruntius, West Humorum, and

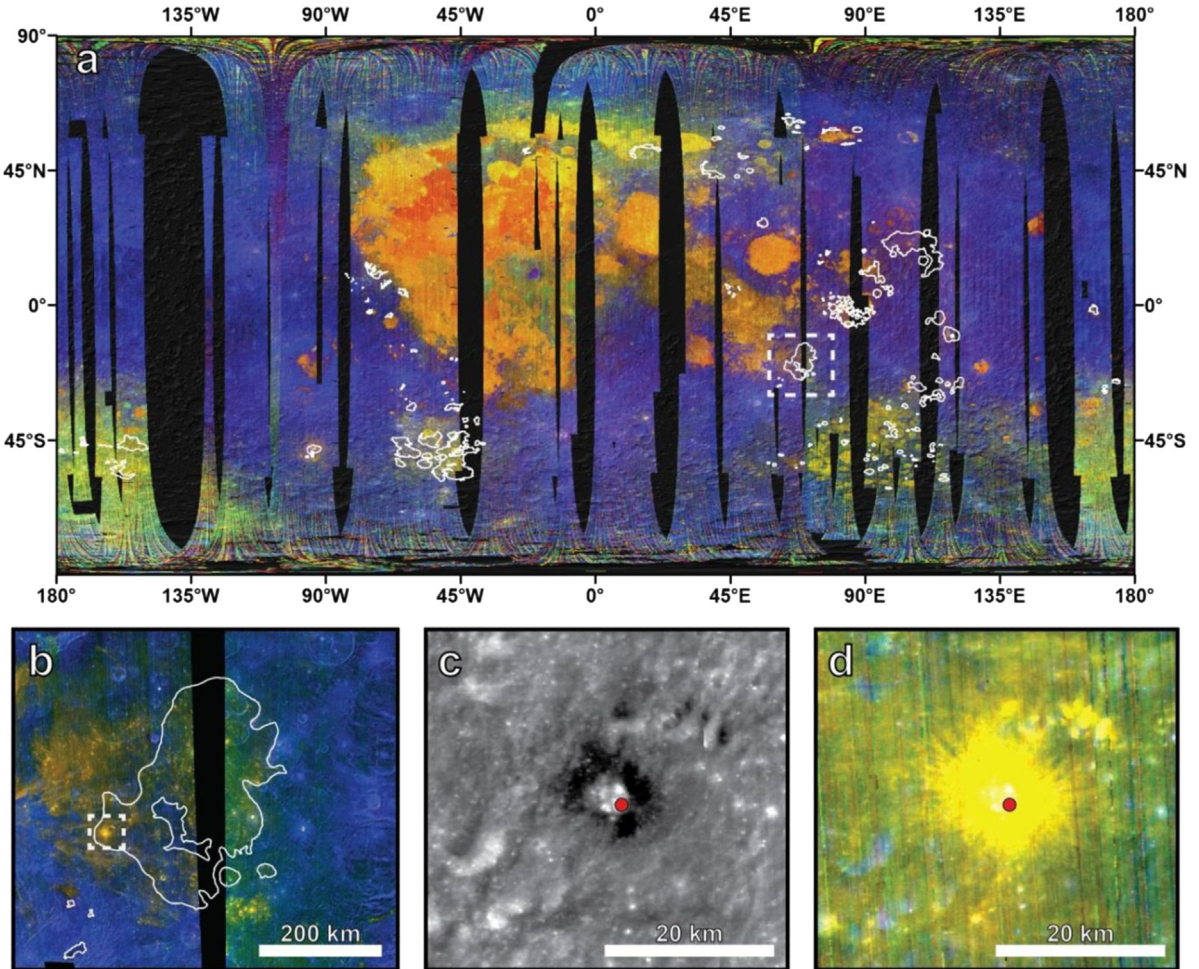


Fig. 1. Mapped cryptomaria and dark-halo impact craters (DHCs). (a) Global color composite of OP2c1 M^3 data (R: 1 μm integrated band depth, G: 2 μm integrated band depth, B: 1489 nm reflectance). Pyroxene-rich deposits appear yellow and orange, while anorthosite-rich material is blue. The locations of cryptomaria are indicated by white polygons. Dashed white box denotes the location of (b). Lunar Orbiter Altimeter 128 pixel/ $^\circ$ hillshade map overlain by M^3 data at 10 km/pixel. (b) High-resolution M^3 (140 m/pixel) mosaic of the Balmer cryptomare (white polygons). Individual DHCs sampled to determine the deposit mineralogy can easily be identified in this dataset. Dashed white box shows the location of parts (c) and (d). (c) A 4.5 km diameter DHC in M^3 1489 nm reflectance image. Low albedo material is excavated from below a high albedo surface material. (d) M^3 color composite (R: 1 μm integrated band depth, G: 2 μm integrated band depth, B: 1489 nm reflectance) of the same DHC in part (c) showing that the crater walls and ejecta deposit are composed of pyroxene-rich materials. Red dot in (c) and (d) denotes the sample location in this particular DHC. (For interpretation of the references to color in this and all subsequent figures, the reader is referred to the web version of this article.)

West Procellarum were used for the optical period 1b–2c1 comparisons.

2.2. Continuum removal

The spectral slope (continuum) was removed prior to calculating the absorption band centers. Lunar spectra have a characteristic red-sloped continuum that is, in part, a product of space weathering processes (e.g., Pieters et al., 1993). In order to accurately model the wavelength position of mineral absorption bands the spectral continuum must be removed (e.g., Sunshine et al., 1990; Hiroi et al., 2000). There is, however, no uniquely defined analytical expression for the lunar continuum (Hiroi et al., 2000; Noble et al., 2006). For this study we chose to remove the continuum before processing the spectra with the MGM to ensure there would be no egregious continuum misfits, such as a fitted continuum intersecting an input spectrum, and to ensure the continuum removal process was consistent for all spectra. Initial MGM analyses of the M^3 spectra collected in this study which used the built-in MGM continuum removal process were unsuccessful; many spectra were modeled with a continuum that intersected the spectrum, resulting in large RMS errors. It was found that the best way to avoid this problem was to remove the continuum prior to

MGM analysis, a result consistent with previous researchers (Isaacson et al., 2011a).

The M^3 spectra were fit with a two-part linear continuum in wavelength space; one part of the continuum was fit over the 1 μm absorption band and the second part was fit over the 2 μm absorption band. Three tie points were selected for continuum removal (Fig. 2). Once selected, the reflectance values for the wavelength immediately long and short of the tie point, in addition to the reflectance of the selected tie point, were averaged together to determine the tie point reflectance value. For example, if tie point 1 was located at 750 nm the reflectance values of the spectrum at 730, 750, and 790 nm were all averaged to produce the reflectance value for tie point 1. Tie point 1 (Fig. 2) was fixed at 0.75 μm , while tie points 2 and 3 were allowed to vary. Continuum tie points 2 and 3 were selected from within a defined wavelength range using the convex hull method. For each spectrum, tie points were chosen as follows: tie point 2 was confined to wavelengths between 1.329 μm and 1.778 μm and tie point 3 was assigned to be longer than 2.776 μm . The convex hull method was used to automatically choose the maximum reflectance values on each side of both the 1 μm and 2 μm absorption features. A straight line was then fit between the reflectance values of tie points 1 and 2 and between tie points 2 and 3. In order to produce a single,

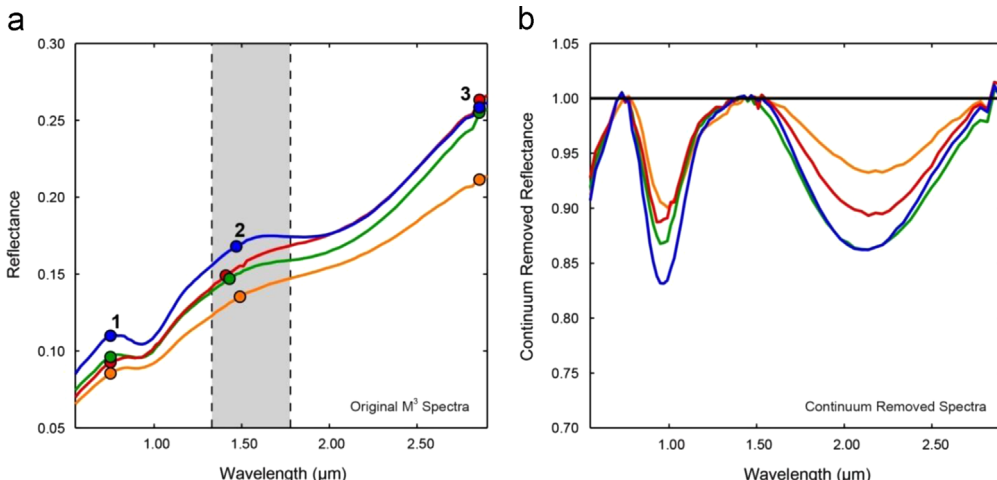


Fig. 2. Automated continuum removal process for M^3 spectra. (a) Original OP2c1 M^3 spectra collected from DHCs in the Balmer cryptomaria. Numbers indicate the three tie points used to remove the continuum over the 1 μm and 2 μm absorption features. Tie point 1 is fixed at 0.75 μm while tie points 2 and 3 are allowed to vary. Gray region highlights the wavelength range used to calculate the position of tie point 2. (b) Continuum removed spectra from the Balmer cryptomaria.

continuum-removed reflectance spectrum, the reflectance values across shorter wavelengths of each spectrum were divided by the linear fit over the 1 μm absorption and the reflectance values across longer wavelengths were divided by the 2 μm linear fit. This continuum-removed spectrum was then input into the MGM in order to calculate the 1 μm and 2 μm absorption band centers.

2.3. Mineralogical analysis

The mineralogy of the cryptomaria was determined using the MGM, an inverse model that deconvolves an individual spectrum into a continuum and a series of modified Gaussian curves approximating electronic absorption features observed within minerals (Sunshine et al., 1990; Sunshine and Pieters, 1993). In total 414 spectra (Tables S1 and S2) were processed to determine the mineralogy of the mapped cryptomaria (Fig. 1a). All collected spectra are dominated by a pyroxene absorption signature with strong 1 μm and 2 μm features. Orthopyroxenes (low-Ca pyroxene), associated with noritic lunar rocks, have short wavelength 1 μm and 2 μm absorption features near 0.9 μm and 1.9 μm (Adams, 1974; Cloutis and Gaffey, 1991; Klima et al., 2007); clinopyroxenes (high-Ca pyroxene) have 1 μm and 2 μm absorptions features at wavelengths longer than 0.95 μm and 2.05 μm (Adams, 1974; Cloutis and Gaffey, 1991; Klima et al., 2011), which dominate the spectral signature of mare basalts. In order to determine the dominant pyroxene signature in the cryptomaria, the M^3 spectra (0.541–2.976 μm) were modeled assuming that only a single pyroxene composition is present. The presence of two pyroxenes of distinct compositions would produce wider absorption features. Therefore, even if the M^3 instrument measured compositionally zoned or two distinct pyroxene minerals on the lunar surface, MGM can still be used to determine the average pyroxene composition (Sunshine and Pieters, 1993) and aid in detecting mineralogic variations within or between cryptomare deposits.

Continuum-removed spectra were processed using the MGM with four absorption features. Three modified Gaussian bands were used to approximate the pyroxene crystal field bands at 1 μm , 1.2 μm , and 2 μm . The fourth band (0.35 μm) was used to describe the metal–oxygen charge transfer absorption in the visible part of the spectrum (Fig. 3, blue Gaussians). Gaussian band centers can be assigned to wavelengths outside of the spectrum wavelengths so that partial absorption features, such as the one at 0.35 μm , can still be modeled. Since the spectral continuum is removed prior to MGM processing the slope parameter in the model is held constant to ensure a flat continuum for

each spectrum (Fig. 3, red horizontal line). The same MGM initialization parameters (Figs. 3a and S2) were used for all processed spectra in order to maintain consistency between model results and to automate the band center calculations. Since the MGM is sensitive to the model initialization parameters (Kanner et al., 2007; Clenet et al., 2011) the initialization parameters used in this study were optimized to model lunar pyroxenes associated with mare basalts, having sufficient Fe^{2+} in the mineral structure to produce 1 μm and 2 μm pyroxene absorption features of comparable strength. This type of modeling is sufficient to: (1) search for variations in pyroxene composition within a particular cryptomare region, and (2) to identify differences in pyroxene composition between all of the mapped cryptomaria (Fig. 1a). The calculated 1 μm and 2 μm band centers were compared with absorption band positions for a suite of low- and high-Ca synthetic pyroxenes (Klima et al., 2007, 2011) to characterize the mineralogy of the cryptomaria.

2.4. Compositional analysis

In addition to mineralogical analyses, the mapped cryptomaria were analyzed using Lunar Prospector gamma-ray spectrometer (LP GRS) Th (ppm) and FeO (wt%) data (Lawrence et al., 1998; Prettyman et al., 2006; Prettyman, 2012). Both of these compositional datasets have an LP GRS resolution at 2°/pixel ($\sim 60 \text{ km}/\text{pixel}$ at the equator). The FeO and Th values were employed to estimate better the lithology of the mapped cryptomaria. LP GRS pixels contained within the cryptomaria boundaries were used to calculate an average value for the entire deposit; LP GRS pixels are too large to measure the composition of individual DHCs. While VNIR data provide information about the spectrally dominant mineralogy, LP GRS Th measurements can provide information about the abundance of incompatible elements in the rock and will help to distinguish between lithologies with a high abundance of incompatible elements, such as the Mg-suite ($< 5 \text{ ppm}$) (Wieczorek et al., 2006) and KREEP basalts (5–15 ppm; Apollo 15 extrusive KREEP basalts have 10–11 ppm) (Lucey et al., 2006; Wieczorek et al., 2006), and those rock types with a lower concentration of incompatible elements (i.e., mare basalts, $< 1 \text{ ppm}$ on average) (Korotev, 1998). FeO measurements can also provide more precise estimates of the iron content than the VNIR spectral data and will be useful for distinguishing between iron- and magnesium-rich rocks.

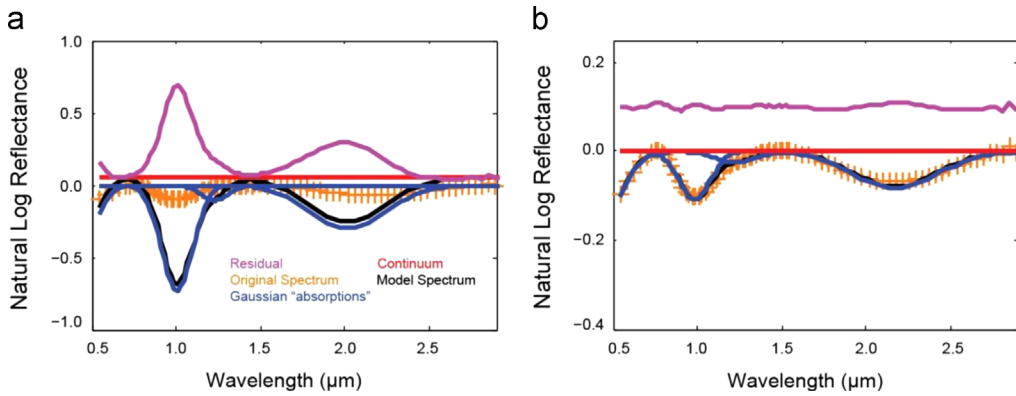


Fig. 3. An example of the Modified Gaussian Model (MGM) fitting routine. (a) The initial conditions of the model: the orange '+' outline the input spectrum, the red horizontal line is the continuum, the four blue Gaussians show the starting position and shape of the modeled pyroxene absorption features (see Section 2.3.), the modeled spectrum in black, and the residual in pink. The four blue Gaussians and the black model spectrum represent the initial conditions chosen for the automated MGM developed in this study to process 100s of spectra at a time. The Gaussian centered at 0.35 μm is only partially visible; its long wavelength end can be seen to the far left of both graphs. (b) The results produced by the MGM fitting routine. The residual (pink line) shows that the MGM has iteratively positioned and sized the Gaussians to best fit the input spectrum (orange '+'). The ordinate is scaled differently in part (b) in order to show the position of the fitted Gaussians and residual values.

3. Results: Modified Gaussian Model mineralogies

3.1. Comparison with synthetic pyroxenes

In order to test whether our model produces accurate results, the synthetic pyroxene spectra of Klima et al. (2007, 2011) were processed using the same continuum removal process and MGM input parameters used for the M³ spectra. Orthopyroxene spectra are accurately modeled using the methods outlined above (Section 2) (Fig. 4, red squares). The modeled synthetic clinopyroxene data plot to the left of the synthetic pyroxene trend; most of the 1 μm values agree well with the Klima et al. (2007, 2011) measurements, while the 2 μm absorption features are modeled at shorter wavelengths (Fig. 4, blue squares). Of the clinopyroxenes, the augite spectra (Fig. 4, bottom right blue squares) were modeled the most accurately followed by the diopsides and hedenbergite spectra (Fig. 4, top right blue squares). The modeled diopside and hedenbergite clinopyroxene spectra had both short 1 and 2 μm absorption features while the augite spectra were modeled with only a short 2 μm absorption feature.

The discrepancy between the modeled band center values from this study and those of Klima et al. (2007, 2011) can be explained by differences in the assigned continuum. Variation in absorption band center due to the continuum removal process has been previously noted (Clenet et al., 2011). Klima et al.'s (2007, 2011) laboratory spectra of the synthetic pyroxenes were measured from 0.45 to 2.6 μm; in many cases, the entire 2 μm absorption band was not measured which, in our continuum removal process and MGM modeling, shifts the band center of the 2 μm absorption features to shorter wavelengths (Fig. 4).

This comparison between Klima et al. (2007, 2011) band center values and those values derived from our automated MGM indicates that the model developed in this study can be used to differentiate between different pyroxene types and compositions. There are limitations to our model; the automated MGM calculates a short wavelength 2 μm absorption feature (Fig. 4). While the model is not able to calculate the actual 1 μm and 2 μm band centers, the calculated 1 μm and 2 μm band centers can be compared relative to one another in order to distinguish between different pyroxene mineralogies.

3.2. Optical period comparison

Data from the three different M³ optical periods (1b, 2c1, and 2c2) analyzed in this study do produce different average band

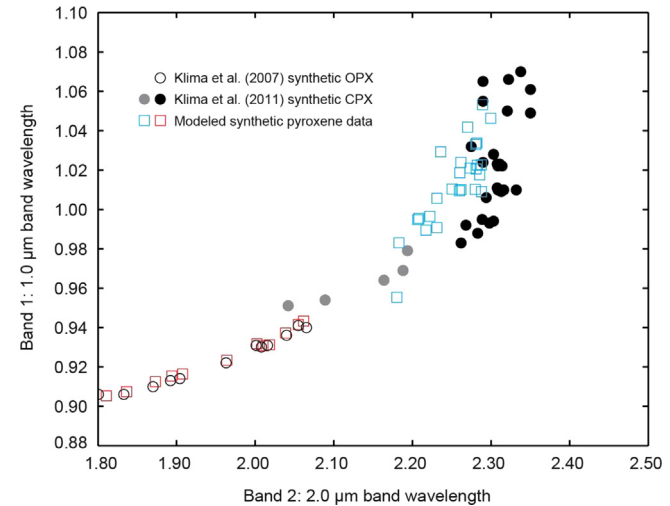


Fig. 4. Comparison of the model results from this study to the Klima et al. (2007, 2011) synthetic pyroxene suite on a plot of the position of the 1 μm and 2 μm absorption features (McCord and Adams, 1973). Red squares are the modeled orthopyroxene results from this study, which agree well with the band center values from Klima et al. (2007). Blue squares represent the clinopyroxene modeled values from this study. The gray dots denote unpublished pigeonite-rich pyroxene spectra that were not modeled in this study.

center positions for the 1 μm, 1.2 μm, and 2 μm absorption features respectively (Fig. 5, Table 1). Optical period 2c1 was used initially to analyze spectra collected from DHCs in cryptomaria and fresh craters within exposed maria from the same study region (i.e., sampling spectra in Schiller–Schickard cryptomaria and Schiller–Schickard exposed maria). In order to estimate the uncertainty in the calculated band centers from optical period 2c1, it was necessary to determine the variability in the band center calculations due to spacecraft temperature variations and M³ instrument uncertainties. This task was accomplished by comparing modeled band centers for spectra collected from the same location in two different M³ optical periods. Optical periods 2c1 and 1b had 15 overlapping spectra locations, while optical periods 2c1 and 2c2 shared 89 spectra locations.

The 1.2 μm absorption feature has the least amount of variation between optical periods, approximately 2 nm (Fig. 5c and d; Table 1). The mean difference between the 1.2 μm absorption

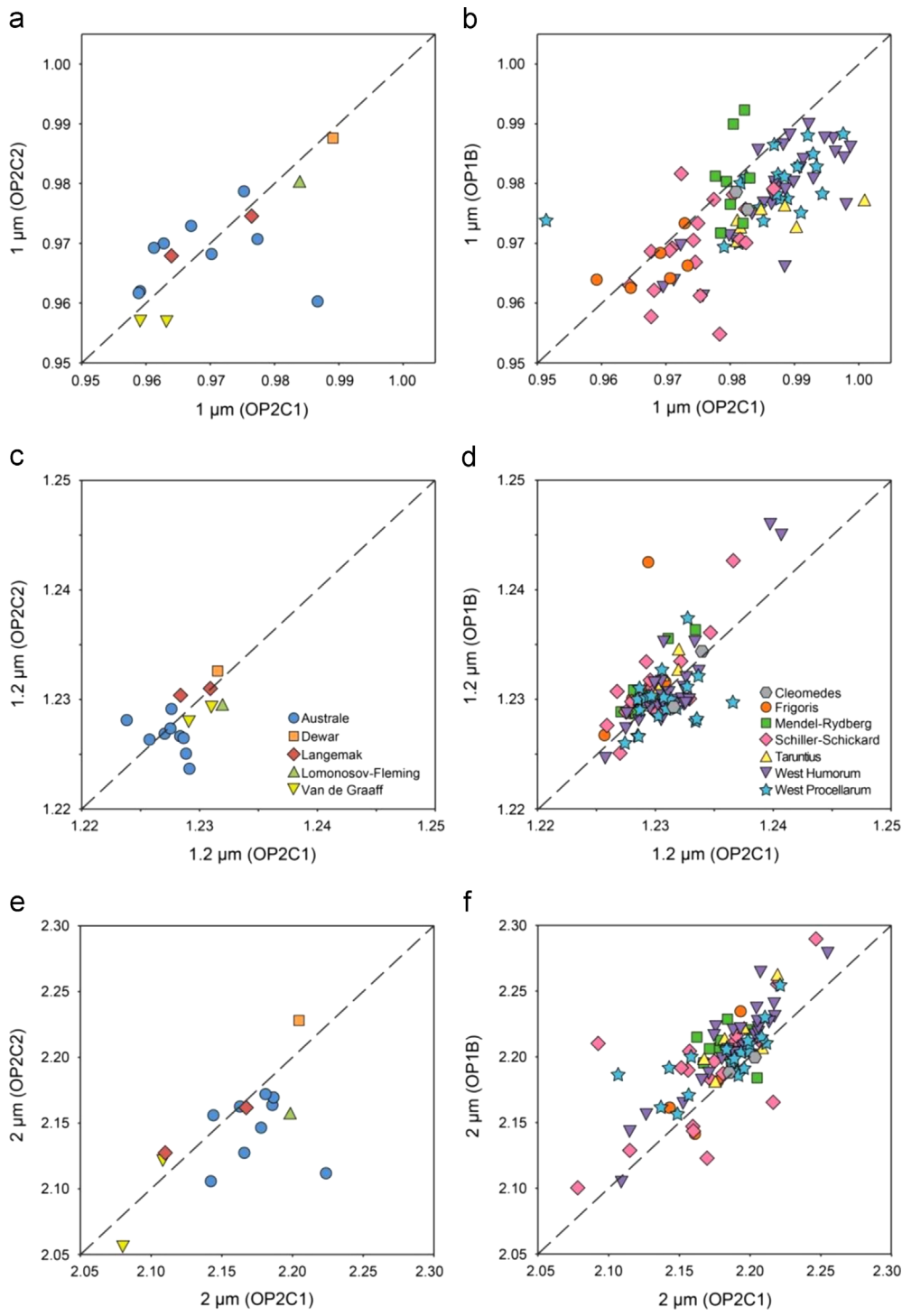


Fig. 5. Comparison of calculated band centers ($1\text{ }\mu\text{m}$, $1.2\text{ }\mu\text{m}$, and $2\text{ }\mu\text{m}$) from three different M^3 optical periods, 1b, 2c1, and 2c2. Spectra collected from the same location in two datasets were processed using the MGM to compare calculated absorption band centers. The observed variation in band centers between M^3 optical periods can be used to estimate the error of these measurements. Data collected during optical period 2c1 have the largest areal extent and cover at least a portion of all mapped cryptomaria. Thus, these data are considered as the baseline from which 1b and 2c2 values will be compared. (a) Calculated $1\text{ }\mu\text{m}$ band centers in OP2c1 versus OP2c2; (b) calculated $1\text{ }\mu\text{m}$ band centers in OP2c1 versus OP1b; (c) calculated $1.2\text{ }\mu\text{m}$ band centers in OP2c1 versus OP2c2; (d) calculated $1.2\text{ }\mu\text{m}$ band centers in OP2c1 versus OP1b; (e) calculated $2\text{ }\mu\text{m}$ band centers in OP2c1 versus OP2c2; and (f) calculated $2\text{ }\mu\text{m}$ band centers in OP2c1 versus OP1b. Legend for each column is shown superposed on the $1.2\text{ }\mu\text{m}$ graphs.

band center in the 1b–2c1 and 2c2–2c1 optical period comparisons was almost identical at 1.9 nm and 1.8 nm, respectively. In comparison, the $1\text{ }\mu\text{m}$ absorption mean difference is slightly larger ($5.8 \pm 4.0\text{ nm}$; Table 1). Optical periods 1b and 2c1 showed a larger discrepancy in the calculated $1\text{ }\mu\text{m}$ band center values (8.1 nm), compared to 2c2 and 2c1 (3.5 nm). The $2\text{ }\mu\text{m}$ absorption band had,

by far, the most variable calculated band center values with a mean difference of $25.4 \pm 9.8\text{ nm}$ for all optical periods. The mean difference for the 2c2–2c1 comparison is slightly larger than for the 1b–2c1 comparison (Table 1). The measured variability in the $1\text{ }\mu\text{m}$ and $2\text{ }\mu\text{m}$ band centers are within the observed uncertainty of the MGM (Kanner et al., 2007) and the mean differences

Table 1

Mean difference in calculated 1, 1.2, and 2 μm absorption features between the different M^3 optical periods (1b versus 2c1; 2c2 versus 2c1).

	Optical period	Band center difference (nm)
1 μm	1b, 2c1	8.1
	2c2, 2c1	3.5
	Mean of all 3 optical periods	5.8 \pm 4.0
1.2 μm	1b, 2c1	1.9
	2c2, 2c1	1.8
	Mean of all 3 optical periods	1.9 \pm 0.8
2 μm	1b, 2c1	24.3
	2c2, 2c1	26.3
	Mean of all 3 optical periods	25.3 \pm 9.8

(Table 1) are significantly smaller than the actual range of calculated band center values (~ 70 nm and ~ 250 nm), supporting the interpretation that the observed band center variations represent real mineralogic variations.

There are more spectra with the same M^3 spectral coverage in optical periods 1b and 2c1 compared with optical periods 2c2 and 2c1 (15 versus 89; Fig. 5, cf. left column with right column). The mean difference in calculated band centers observed between 2c2 and 2c1 appears random as there are no clear systematic trends observed for the 1 μm , 1.2 μm , or 2 μm absorption features (Fig. 5a, c, and e). For the 1 μm and 1.2 μm absorption features the data are evenly distributed around a 1:1 line, but for the 2 μm absorption band center 2c2 either produces short wavelength band centers or 2c1 measurements result in long wavelength band centers. The paucity of overlapping data points in 2c2 and 2c1 could potentially obscure any clear relationship between these two optical periods.

The abundance of overlapping data in optical periods 1b and 2c1 enables a more robust comparison of the calculated band centers. Similar to the 2c2–2c1 comparisons, the 1.2 μm band center does not show any systematic variation between 1b and 2c1 (Fig. 5d). Conversely, the 1 μm and 2 μm absorptions do show systematic, but contradictory, variations. If optical period 2c1 is taken as the baseline dataset, then the wavelengths of the 1 μm band centers calculated for the 1b data are too short (Fig. 5b). The reverse is true for the calculated 2 μm band centers (Fig. 5f); the 1b 2 μm band centers calculated using the MGM are located at longer wavelengths compared with the 2c1 data. If these band center variations were due to actual mineralogic differences the band centers of the 1 μm and 2 μm absorption features would both shift to long or short wavelengths in tandem.

The M^3 instrument was above its nominal operating temperature (156 K) for most of the mission. During the “hot” optical periods, such as 2c1 and part of 2c2 (May 20–July 9, 2009), temperatures exceeded ~ 160 K (Green et al., 2011). “Cold” optical periods occurred when the instrument was below ~ 160 K and include optical periods 1b and part of 2c2 (July 12–August 16, 2009). Variations in detector temperatures affect the shape of spectra as evidenced by the need to generate two different ground truth corrections, one for “hot” and one for “cold” data (Isaacson et al., 2013). “Hot” data deviated more from the laboratory-measured spectra compared with the “cold” data. The application of the ground truth correction brought the 1 μm band position of “hot” and “cold” spectra closer together, such that at lower latitudes they are almost identical. It is only at higher latitudes that a deviation in the shape of spectra occurs (Isaacson et al., 2013). Therefore, smaller spectral variations are expected in the 1 μm region due to the applied ground truth corrections and the minimal contribution from thermal effects at wavelengths

$< \sim 1.5 \mu\text{m}$. Smaller variations in the position of the 1 μm are, in fact, observed (Fig. 5; Table 1).

The 2 μm variations between optical periods are much more substantial and are difficult to attribute to one particular variable. A comparison of the MGM-derived 2 μm positions with M^3 detector temperatures suggests that there is no correlation between the two variables (Fig. 5e and f); optical period 2c1 is “hot” and 2c2 is both “hot” and “cold” (Table S3). In the 2c2–2c1 comparison (Fig. 5e), 2c1 is either producing long wavelength 2 μm band centers, or 2c2 band centers are too short. On the other hand, the 1b–2c1 comparison (Fig. 5f) suggests that 2c1 produces short wavelength 2 μm absorptions, or 1b band center values are too long. Thus, the “hot” 2c1 data produce MGM 2 μm absorptions that occur at both long and short wavelengths. The Dewar and Van de Graaff data can be used to confirm this observed lack of a correlation; Dewar and Van de Graaff are the only “cold” 2c2 data in this study, the remaining 2c2 data are from “hot” detector periods. While the Dewar 2c2 datum plots above the 1:1 line (Fig. 5e, orange square), just like the “cold” 1b data (Fig. 5f), the Van de Graaff 2c2 data plot both above and below the 1:1 line (Fig. 5e, yellow upside down triangle), providing no clear relationship between “hot” 2c1 and “cold” 2c2 data. Thus the “cold” 2c2 data provide more evidence to suggest that detector temperature may not be controlling the 2 μm band center variations.

These M^3 optical period comparisons of 1 μm and 2 μm band center data indicate that the variation is not directly related to temperature and should not systematically affect MGM results, providing confidence that M^3 spectra can be used to distinguish between the presence of low- versus high-Ca pyroxene.

3.3. M^3 cryptomaria and maria

The calculated mineralogies of the 414 measured cryptomare and exposed mare spectra overlap substantially with one another (Fig. 6). Cryptomaria and exposed maria display a spread in band center values, from 0.95 to 1.00 μm and 2.05 to 2.30 μm . The 1 μm , 1.2 μm and 2 μm band centers produce band center ranges of 72 nm, 30 nm, and 256 nm, respectively. Despite the variation in band center values, all of the M^3 remote measurements overlap with well-characterized synthetic clinopyroxene samples measured in the laboratory (Figs. 6 and 7). Additionally, there is a strong correlation between the position of cryptomare and mare band center values and band center measurements derived from Apollo 11, 12, and 15 rock and soil samples (McCord and Adams, 1973) (Fig. 6, gray fields).

In 83% of study regions there is no clear distinction between the MGM-derived band center values for cryptomaria and exposed maria (Fig. 7). The few cryptomare regions that do show some distinction between cryptomaria and exposed maria mineralogies include Langemak, Lomonosov–Fleming, and Lacus Solitudinis (Fig. 7h, i, q). Cryptomaria in Lacus Solitudinis (Fig. 7q) generally have longer wavelength 1 μm and 2 μm absorption features compared with the exposed maria. The reverse is true for the Langemak (Fig. 7h) and Lomonosov–Fleming (Fig. 7i) regions; cryptomaria have shorter wavelength 1 μm and 2 μm absorption bands. Despite this observed separation between cryptomaria and exposed maria, there is some overlap between the cryptomare and exposed mare band centers around Lacus Solitudinis and Lomonosov–Fleming.

Frigoris, Hercules, and Tarunitus are relatively “young” cryptomaria, formed from the continuous ejecta deposits of Eratosthenian- and Copernican-aged craters overlying and partially covering exposed maria (Wilhelms and McCauley, 1971; Giguere et al., 2003), compared with the impact basin events that formed the larger cryptomaria. The formation mechanism for relatively “young” cryptomaria (Giguere et al., 2003) implies that the

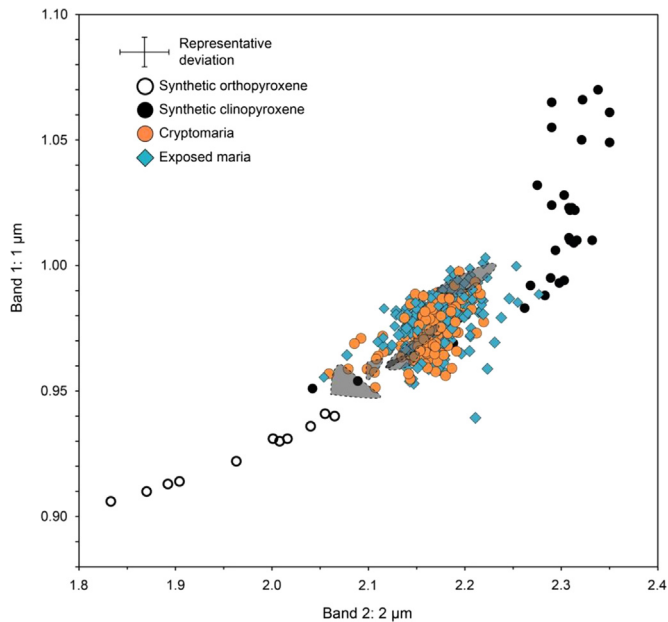


Fig. 6. Position of the 1 μm and 2 μm absorption features (McCord and Adams, 1973) for all cryptomare (orange circles) and exposed mare deposits (blue diamonds). The data are overlaid on laboratory measurements of a suite of well-characterized synthetic pyroxenes (Klima et al., 2007, 2011) and overlaid by five gray fields representing measurements of Apollo 11, 12, and 15 rock and soil samples (McCord and Adams, 1973). All collected spectra, cryptomare and mare, coincide with the synthetic clinopyroxene 1 μm and 2 μm absorption positions. The location of the data cloud at the lowermost portion of the clinopyroxene trend is consistent with pigeonite (Klima et al., 2011). Error bars are the mean differences in calculated band centers between the different M^3 optical periods (Fig. 5; Table 1). All data are from OP2c1, except for the Milne cryptomare and Van de Graaff mare (OP2c2) because these deposits were not imaged during OP2c1. Representative error bars for the maria and cryptomaria data are displayed in the legend as “representative deviation”.

exposed mare deposits should have the same composition as the cryptomare DHCs. MGM-derived 1 μm and 2 μm band centers for Frigoris, Hercules, and Taruntius do have similar cryptomare and mare band center values and, therefore, support the abovementioned formation hypothesis (Fig. 7e, f, and p). Hercules is a clear example of the overlap in MGM-derived band center values between cryptomaria and exposed maria (Fig. 7f).

Schiller–Schickard and West Humorum show large variations in the mineralogy of both cryptomaria and exposed maria (Fig. 7m and s), on the order of 0.015–0.045 μm and 0.115–0.225 μm for the 1 μm and 2 μm absorption bands, respectively. The short wavelength end of the calculated absorption band centers corresponds to low-Ca pigeonites and the longer wavelength end of the trend corresponds to low-Ca augites. Other study regions, such as Smythii and South Pole–Aitken, do not display significant mineralogic differences (Fig. 7n and o), with <0.025 μm and <0.070 μm variation for the wavelength position of the 1 μm and 2 μm absorption bands, respectively. Many study regions have large data clouds with no distinct mineral trends; the numerous observations from Austral produce a large data cloud with <0.05 μm variation in the calculated position of the 1 μm absorption band, and 0.1 μm variation in the 2 μm absorption band (Fig. 7a).

An increase in the relative abundance of orthopyroxene to clinopyroxene, due to mixing of basin ejecta materials with the DHC-excavated material, in certain mare and cryptomare ponds might explain the large band center variations observed in Schiller–Schickard and West Humorum. However, this explanation is probably not responsible for the absorption band centers

because the variability is also observed in the maria where sampled craters do not impact into any high albedo feldspathic materials and, therefore, do not have the opportunity to mix with substantial quantities of orthopyroxene-rich materials. In an attempt to prevent collecting cryptomaria spectra from regions of mixed materials, only the interior walls of DHCs were sampled, where regolith cannot accumulate and cover rock outcrops. If mixing processes are responsible for the variation in band centers it should be observed at Schiller–Schickard because these cryptomaria were covered by ejecta from one of the youngest impact basins on the Moon, Orientale. Cryptomaria closest to the Orientale basin rim would have more superposed Orientale ejecta and are expected to mix with a larger amount of orthopyroxene-rich ejecta, while cryptomaria further away would have less material to mix with and, therefore, have longer wavelength absorptions due to the dominance of basaltic material. This spatial trend is not observed in the data and suggests that another geologic process is responsible for the observed band center variations.

Additionally, the variation in pyroxene composition at Schiller–Schickard and West Humorum is probably not related to the evolution of the magma source region over time because the same trend is observed for both old (cryptomare) and young (mare) volcanic deposits. If the magma source did evolve then the maria and cryptomaria band centers should be separated from one another, instead of overlapping. In order to be detected in M^3 spectra, the different pyroxene compositions need to be generated by a process that is active over spatial scales of hundreds of meters (the minimum M^3 pixel is 140 m). Compositional anomalies in the lunar mantle due to cumulate overturn are estimated to be on the order of 10^2 – 10^4 m (Spera, 1992), well below the total distance covered by the Schiller–Schickard (750–850 km) and Western Humorum (600–725 km) basalt deposits and above the M^3 detection limits. Thus, a heterogeneous source region for the magmas erupted in the Schiller–Schickard and West Humorum regions may provide a possible explanation for the observed pyroxene variations.

Most of the observed mineralogic variation is in the 2 μm absorption band. For all processed spectra, both cryptomaria and exposed maria, the wavelength position of the 1 μm absorption band has a much narrower range of calculated values. The larger observed variation at 2 μm is consistent with the measured band center variations between the different M^3 optical periods (Table 1, Fig. 5). Laboratory measurements of synthetic and natural samples (Cloutis and Gaffey, 1991; Klima et al., 2007, 2011) have ~ 170 nm variation in the position of the 1 μm band and ~ 525 nm of variation in the 2 μm absorption band between ortho- and clinopyroxenes. Of the three crystal field absorptions modeled, the 2 μm band has the largest uncertainty between the different M^3 optical periods, ± 25.3 nm which is the error value assigned to each data point in Figs. 6 and 7. The uncertainty associated with the 1 μm absorption feature is only ± 5.8 nm (Table 1), approximately four times smaller. The variability and uncertainties in the calculated band center values also coincide with the change in spectral resolution of the M^3 data from the 1 μm region to the 2 μm region. Between ~ 730 nm and ~ 1550 nm the M^3 imaging spectrometer has a spectral resolution of 20 nm. At longer wavelengths, from 1580 to 2500 nm the spectral resolution decreases to 40 nm (Green et al., 2011). Thus, there are more data points available in the 1 μm region to constrain the position of the absorption feature compared with the 2 μm region. The smaller range in the position of the 1 μm absorption band in synthetic and natural pyroxenes, combined with the higher M^3 spectral resolution in the 1 μm region produce a narrower range of MGM-derived 1 μm band center values for the spectra sampled in this study. Conversely, the greater observed variability in the MGM-derived 2 μm band centers is a result of lower M^3 spectral resolution and

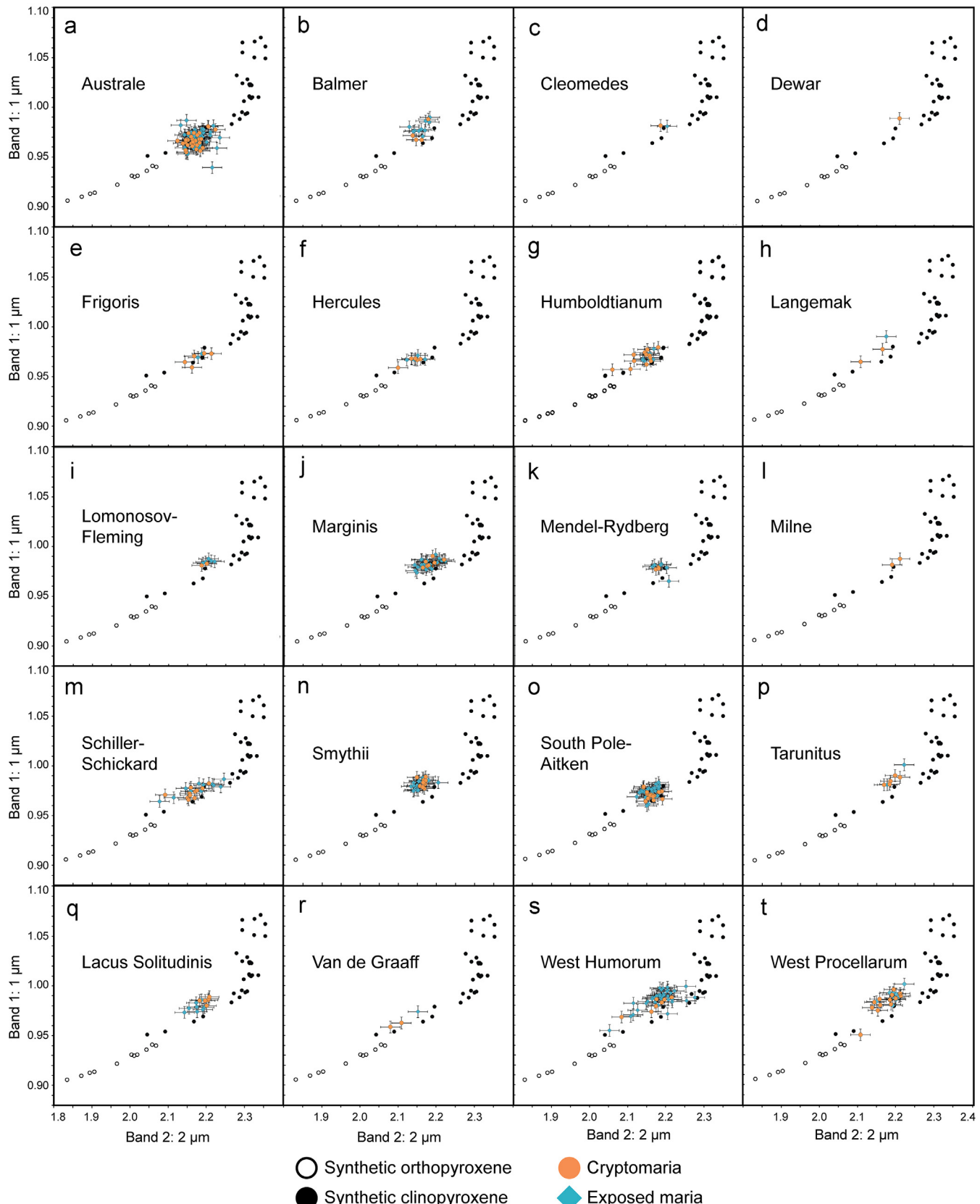


Fig. 7. Wavelength positions of the 1 μm and 2 μm absorption features for each individual study region. Cryptomaria (orange circles) and exposed mare (blue diamonds) from each study region are plotted against a suite of synthetic pyroxenes (Klima et al., 2007, 2011). (a) Australe, (b) Balmer, (c) Cleomedes, (d) Dewar, (e) Frigoris, (f) Hercules, (g) Humboldtianum, (h) Langemak, (i) Lomonosov-Fleming, (j) Marginis, (k) Mendel-Rydberg, (l) Milne, (m) Schiller-Schickard, (n) Smythii, (o) South Pole-Aitken, (p) Taruntius, (q) Lacus Solitudinis, (r) Van de Graaff, (s) West Humorum, and (t) West Procellarum. All data are from optical period 2c1, except for Milne cryptomaria and Van de Graaff mare, which are 2c2. Legend for all graphs is located at the bottom of the figure.

large variations in natural and synthetic pyroxene 2 μm absorption band centers.

A majority of the calculated band centers plot to the left of the synthetic pyroxene trend (Fig. 5b, g–j, n, and p–s). Typically, when data plot off of the pyroxene trend it indicates that more than one mineral phase is present (Adams, 1974). The presence of other minerals may play a role in the band center results from this study because lunar rocks contain many minerals in addition to pyroxene, including olivine, plagioclase, and other minor phases (e.g., ilmenite and spinel), that could influence the shape of the spectrum. For instance, plagioclase has a distinct mineral absorption at 1.25 μm (Conel and Nash, 1970), overlapping substantially with the 1.2 μm pyroxene absorption (e.g., Sunshine et al., 1990; Klima et al., 2008). While both the plagioclase and pyroxene absorption features at $\sim 1.2 \mu\text{m}$ are observable with trace amounts of Fe, pyroxene tends to dominate the spectrum due to its larger imaginary index of refraction (cf. Lucey, 1998; Carli et al., 2014) and can completely mask the plagioclase absorption. As little as 5–10 wt% pyroxene is needed to remove all evidence of crystalline plagioclase in a VNIR spectrum (Cheek et al., 2013) and most lunar basalts have 45–60% pyroxene. Currently, it is difficult to distinguish between a pyroxene spectrum with a strong 1.2 μm absorption and a spectrum of a plagioclase–pyroxene mixture; the geologic setting (e.g., volcanic lava flow versus crater central peak) of most spectral detections usually provides enough evidence to interpret the spectrum.

However, it is more likely that residual thermal effects in the M^3 dataset are influencing the position of the 2 μm absorption band center. A first-order thermal correction was applied to the M^3 data by deriving temperature and emissivity from M^3 spectra and removing the thermal component from near infrared wavelengths (Clark et al., 2011). This thermal correction did improve the shape of M^3 spectra at infrared wavelengths, but in order to completely correct for thermal effects a more complex model incorporating local topographic scattering effects must be developed and applied to the spectra (McCord et al., 2011; Bandfield et al., 2014). Despite the incomplete removal of thermal emission from M^3 spectra, we chose to model the entire M^3 wavelength range (0.540–2.976 μm). A shorter wavelength could be chosen as tie point 3 for the continuum removal process (Section 2.2) to partially combat the thermal effects in the infrared part of the spectrum, but there is no way to ensure that this technique would move the position of the 2 μm absorption band center closer to its original expected value. Therefore, to avoid adding this uncertainty into the calculated band centers, the entire wavelength range of the M^3 spectra was processed. Regardless of the exact wavelength position of the 2 μm absorption band center, all of the cryptomare spectra indicate a clinopyroxene-dominant mineralogy, consistent with a mare basalt composition.

3.4. Compositional data

To further constrain the possible rock types of the mapped cryptomaria (Fig. 1a) the Th (ppm) and FeO (wt%) abundances were estimated using the LP GRS data (Fig. 8). The comparatively low resolution ($\sim 60 \text{ km/pixel}$) of the LP data requires that the average value for an entire mapped cryptomare deposit be used in the derivation of these compositional values. Thus, the reported values are averages of material exposed by DHCs and the feldspathic material superposed on the cryptomare deposit. For all cryptomaria, Th abundances are between 0.5 and 4.8 ppm (Fig. 8), with an average value of 1.4 ppm. The Frigoris cryptomaria have the largest Th concentration (4.8 ppm), followed by West Procellarum and Van de Graaff (2.7 ppm), Hercules (2.4 ppm), and West Humorum (1.9 ppm). All of these cryptomaria are located along the edge of the Procellarum KREEP Terrane (PKT) (Jolliff et al.,

2000), thought to be Th-rich Imbrium basin ejecta (Haskin, 1998), which suggests that these Th values are affected by the concentration of incompatible elements found in this region of the Moon and may not reflect the actual amount of Th in the buried mare deposit. Of the cryptomaria not associated with the PKT, only Dewar, Van de Graaff, and South Pole–Aitken have Th values $> 2 \text{ ppm}$. However, these three regions occur near another Th enriched terrane, the South Pole–Aitken Terrane (SPAT) (Jolliff et al., 2000). The remaining cryptomare have Th values between 1.0 and 1.4 ppm.

Cryptomaria LP GRS FeO values are between 5.4 and 12.4 wt%, with an average of 8.4 wt%. The highest FeO values are generally associated with cryptomaria adjacent to areally extensive mare basalt deposits: Frigoris (12.1 wt%), Hercules (9.2 wt%), Taruntius (12.4 wt%), and West Procellarum (9.5 wt%). Other cryptomaria, however, namely Smythii (10.0 wt%) and South Pole–Aitken (10.3 wt%), also have high FeO values. In the case of Smythii the high FeO is due to its close proximity to extensive mare basalt deposits contained within the impact basin. As mentioned previously, the South Pole–Aitken cryptomaria are within the SPAT, which also has an FeO enrichment. The remaining cryptomaria generally have between 6 and 9 wt% FeO. Dewar has the lowest average FeO value, 5.4 wt%, which may be a function of its isolated location on the farside where, throughout lunar history, this small deposit was probably covered with a substantial layer of feldspathic material due to impact gardening which lowered the FeO content.

Compared with the compositional measurements of lunar rocks, cryptomaria average Th and FeO values are dominantly associated with the Mg-norite and Mg-gabbro values (Fig. 8). It is important to remember that these LP values are mixtures of the underlying basalts and the overlying feldspathic ejecta. The compositional influence of ejecta may bias both the Th and FeO values to overlap with the Mg-norites. Contamination by feldspathic materials has been shown to lower the FeO content of lunar soils (Korotev, 1998). The average FeO content of Schiller–Schickard, in particular, is low at 7.8 wt% (Fig. 8). However, the FeO content of this cryptomare deposit varies from ~ 5 to 10 wt%. These FeO variations can be correlated with the albedo of the surface, where higher FeO values correspond to lower albedo materials. The reverse is also true: high albedo surfaces typically have lower FeO values. This albedo–FeO correlation suggests that cryptomaria with high FeO and low albedo have only a thin layer of superposed basin or crater ejecta. The albedo and FeO variations are consistent with compositional and albedo observations at Schiller–Schickard, a region that was resurfaced by the Orientale basin impact event. The northwestern Schiller–Schickard cryptomaria, closest to the Orientale basin rim and with the thickest superposed ejecta, have the highest albedo and lowest FeO values and the southeastern parts of the Schiller–Schickard cryptomaria, farthest from the basin rim and with the thinnest superposed ejecta, have lower albedo and higher FeO.

4. Comparison with other ancient igneous rocks

All spectra sampled from cryptomaria and exposed maria correspond to lithologies dominated by clinopyroxene (Figs. 6 and 7). A clinopyroxene-rich mineralogy is typically associated with mare basalts while orthopyroxene-rich geologic materials, with pyroxene absorption band centers at shorter wavelengths, denote a noritic composition. Reflectance Experiment Laboratory (RELAB) spectra of Apollo samples (Fig. 9a), such as a low-Ti basalt (15058,276), a high-Ti basalt (70017) (Isaacson et al., 2011b), a dunite (72415,64), a norite (72255,74), a troctolite (76535,17), a high-Al mare basalt (14301,49), and a KREEP basalt (14310,152)

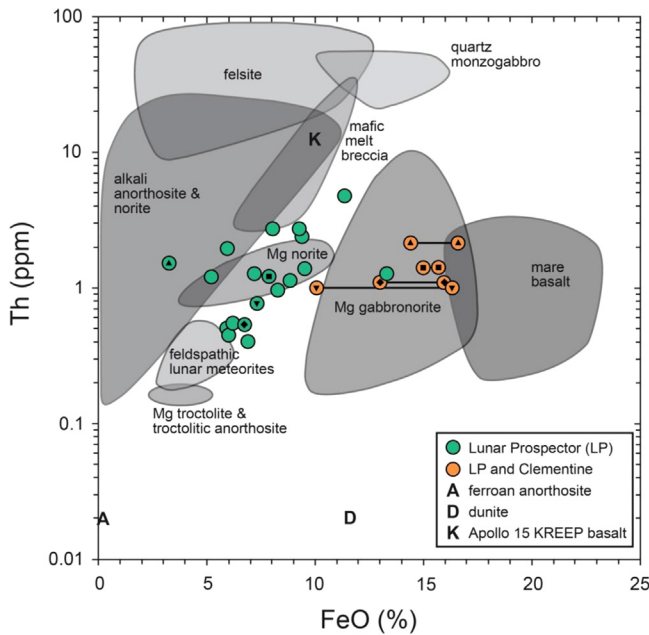


Fig. 8. FeO versus Th values for identified cryptomaria (Fig. 1). Average Lunar Prospector Th (ppm) and FeO (wt%) for an entire mapped cryptomare deposit are plotted in green circles. FeO values of dark-halo impact craters (DHCs) derived from Clementine data (Lucey et al., 1995) and Lunar Prospector Th values measured in previous studies (Giguere et al., 2003; Hawke et al., 2003, 2005; Lawrence et al., 2008) are shown in orange circles. Black horizontal lines connect circles identifying the minimum and maximum values measured for a single cryptomare deposit. Black symbols superposed on circles indicate a specific cryptomare in order to show how the Lunar Prospector FeO values of the entire deposit compare with Clementine FeO values of DHCs: upright triangle=Dewar, square=Balmer, diamond=Schiller-Schickard, upside down triangle=Lomonosov-Fleming. The Th values are not exactly the same between the data collected in this study (green circles) and data from previous studies (orange circles) because the most recent LP calibration (Prettyman, 2012) was used for this study while older calibrations (Lawrence et al., 2002) were used for previous studies. The Lunar Prospector FeO values are low, as would be expected for a basaltic deposit that has been covered and mixed with feldspathic material. After Figure 2.5 from Lucey et al. (2006).

were processed using the same methods as described above (Section 2) for the M^3 spectra, including the continuum removal process. RELAB spectra are bidirectional reflectance measurements (Pieters, 1983) between 0.5 and 2.6 μm . Lunar samples that are not dominated by pyroxene were processed to determine how the automated MGM would fit the spectra of these samples and to test the robustness of the automated MGM and the selected Gaussian wavelength positions.

As expected, the calculated positions of the 1 μm and 2 μm band centers for the lunar rocks show greater variability than the cryptomaria or exposed maria (Fig. 9b). All of these ancient lunar rock types plot off of the synthetic pyroxene trend indicating the complex mineralogy of these rock samples, including minerals other than pyroxene. For instance, the dunite band center results are far removed from the synthetic pyroxene trend (Fig. 9b, green), an expected behavior given that this sample is dominated by olivine and the automated MGM input parameters are optimized for pyroxene spectra. Olivine has three individual absorption features that comprise its 1 μm absorption band (e.g., Burns, 1970), which cannot be modeled accurately with only the two bands assigned to the 1 μm region in our automated MGM. Of all the ancient lunar volcanic rocks, the low-Ti basalt sample plots closest to the band center positions of the M^3 cryptomaria and exposed maria spectra. Each of the modeled lunar rocks are composed of multiple minerals and, therefore, are not accurately

modeled by the single pyroxene approach. However, the model developed here is capable of distinguishing between the different rock types.

5. Discussion

Over time substantial regolith mixing occurs on the Moon, with the uppermost millimeters of the surface (McEwen et al., 1997) overturning more rapidly than deeper parts of the lunar regolith (Gault et al., 1974). The upper microns of the regolith, corresponding to the optical surface viewed by VNIR spectrometers, is overturned within $\sim 10^4$ years. At a depth of ~ 10 cm the turnover rate is on the order of 0.5 Ga (Shoemaker et al., 1970; Gault et al., 1974; McEwen et al., 1997). Thus, the amount of mixing between the basaltic ejecta deposits of DHCs and the underlying feldspathic basin ejecta will depend on the thickness of the DHC ejecta deposits. Thinner DHC ejecta will be mixed with feldspathic ejecta while the thicker regions of the DHC ejecta will be preserved and remain detectable with orbital spacecraft. A DHC in Balmer cryptomaria (Fig. 1c and d) provides a clear example of vertical mixing. The low albedo ejecta halo is confined to within one crater diameter from the rim crest (Fig. 1c). The thinner regions of the ejecta deposit further from the crater rim have been mixed into the surrounding feldspathic regolith, such that a low albedo signature is no longer observable. In M^3 data, however, the pyroxene signature in the mixed regions can be observed and shows the crater ejecta extending outside one crater diameter from the rim crest.

Lateral mixing is also an important process that contributes to homogenization of the lunar regolith (Li and Mustard, 2000). The combination of vertical and lateral mixing diminishes the compositional and spectral signatures of DHCs. Measurements of mare soils collected during the Apollo program indicate that there is less Fe and more Al present compared to the corresponding mare basaltic rocks, providing observational evidence for feldspathic highlands contamination in lunar basaltic soils (Korotev, 1998). The observed offset between the LP GRS FeO and Th values estimated for cryptomaria and the measured FeO and Th values for lunar mare basalts (Fig. 8) can be explained by regolith mixing. The LP GRS data collected for the cryptomaria are averages of the whole deposit (Fig. 8, green circles), both DHCs and basin ejecta deposits, which are more offset from expected mare basalt values compared with the LP GRS Th/Clementine FeO data (Fig. 8, orange circles). The Clementine dataset has a higher spatial resolution (100–200 m/pixel) than LP GRS FeO measurements (~ 60 km/pixel) allowing for the FeO content of individual DHCs to be estimated, instead of calculating the FeO content from the entire mapped cryptomare deposit. Previous researchers have also concluded that regolith mixing has artificially decreased the Th and FeO measurements of cryptomare deposits (Giguere et al., 2003; Hawke et al., 2005; Lawrence et al., 2008).

The geologic setting of each of the ancient lunar rock types included in this study (Fig. 9a) varies and can provide further information to determine the dominant lithology of cryptomaria. Both high-Ti and low-Ti mare basalts are typically located in large impact basins or topographic lows, such as Oceanus Procellarum. The majority of returned samples that have a KREEP basalt composition are actually impact melt rocks associated with the Imbrium formation event. However, there are a few samples from the Apollo 15 and 17 missions that are believed to be extrusive based on a primary igneous texture, a lack of lithic clasts and siderophile elements indicative of meteorite impacts, and evidence for a two-stage cooling process (e.g., 15404, 15358, 15382, 15386, 15434) (Ryder, 1987). It is difficult to infer a geologic setting for many of these samples since they are typically only small hand sample-sized fragments. Despite their small size, suggestions from

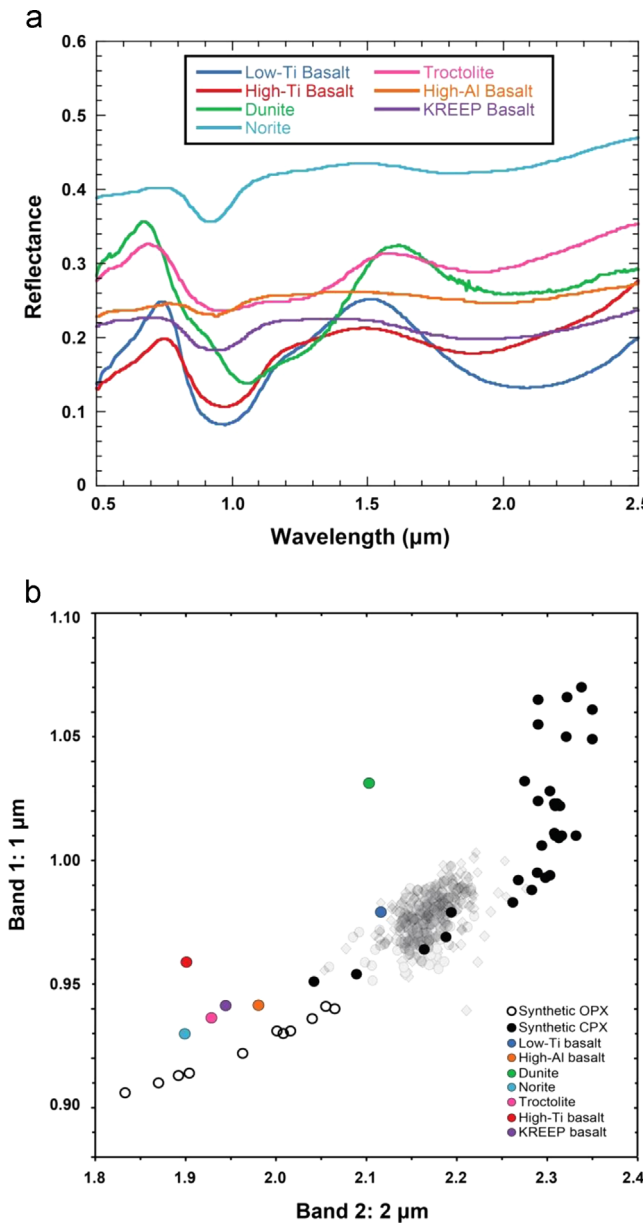


Fig. 9. Spectra of ancient volcanic rock types on the Moon. (a) RELAB spectra of 7 different volcanic lithologies re-sampled to M^3 wavelengths: a low-Ti basalt (15058,276; LR-CMP-152), a high-Ti basalt (70017; LR-CMP-156), olivine clasts from a dunite (72415,64; LS-CMP-003), a norite (72255,74; LS-JBA-212), a troctolite (76535,17; LS-JBA-245), a high-Al basalt (14301,49; LS-JBA-093), and a KREEP basalt (14310,152; LS-JBA-095). Spectra were measured only to 2.5 μm . (b) A 2 μm versus 1 μm plot showing the calculated band positions of the ancient volcanic rocks, using the same method applied to the M^3 orbital spectra. The semi-transparent gray symbols (circles and diamonds) are the cryptomaria and maria MGM results from Figs. 6 and 7; the darker gray regions are areas with a higher density of symbols.

geologic mappers (Cadogan, 1974; Hawke and Head, 1977; Spudis, 1978; Wilhelms, 1987) and the fact that the KREEP samples were collected in basin settings at the Apollo 15 and 17 sample sites indicate that many of the extrusive KREEP basalts may have formed as early basin fill deposits. The density of KREEP and high-Al mare basalts is similar to the latest estimates of the average crustal density (Wieczorek et al., 2013), which would allow these mantle melts to propagate and erupt onto the surface if located within hydrostatically favorable locations, such as impact basins (Solomon, 1975). The high aluminum content of

the KREEP and high-Al mare basalts and their occurrence in Apollo 14 Fra Mauro breccias argues for a similar geologic provenance (Nyquist and Shih, 1992). The identification of in situ troctolite-rich lithologies is confined to crater central peaks (Pieters and Tompkins, 1999; Tompkins and Pieters, 1999). During an impact, the crater central peaks are thought to expose the deepest-seated crustal materials (Ullrich et al., 1977; Melosh, 1989). The fact that troctolite-rich materials are only exposed in crater central peaks suggests that they occur dominantly as intrusive igneous deposits in the lunar crust. Dunite and olivine-rich rocks are also excavated from the crust (Pieters, 1982; Tompkins and Pieters, 1999) and possibly from the mantle during impact basin events (Yamamoto et al., 2010).

The presence of troctolite and dunite lithologies in central peaks and the lack of detections outside of impact craters imply that these rocks occur primarily as plutons and are usually of limited areal extent; this observation is inconsistent with the geologic settings of mapped cryptomaria (Fig. 1a). The most areally extensive cryptomaria are associated with ancient impact basins, such as Schiller-Zucchi and Lomonosov-Fleming, while the remaining deposits are associated with other smaller impact structures. Cryptomaria are detected by the identification of a DHC clinopyroxene mineralogy; high concentrations of DHCs superposed on light smooth plains are indicative of a cryptomare deposit (Whitten and Head, 2015). No cryptomaria have been positively identified on the walls or central peak of a large impact crater or basin. Based on orbital detections of early lunar volcanic rock types, the lithologies expected to erupt as voluminous deposits on the lunar surface include mare basalts (high- or low-Ti magmas), KREEP basalts, and high-Al mare basalts. The observed distribution of these four basaltic lithologies is consistent with the geologic setting of the mapped cryptomaria (Fig. 1a).

Several lines of evidence suggest that the cryptomaria analyzed in this study correspond to a mare basalt mineralogy, including: (1) the dominance of clinopyroxene in the M^3 spectra (Figs. 6 and 7), (2) the overlap of MGM-derived absorption band positions for cryptomaria and exposed mare basalts (Figs. 6 and 7), (3) the band center overlap between Apollo mare samples and the M^3 cryptomaria and maria (Fig. 6, gray polygons), (4) mixing analyses and turnover rates for the lunar regolith explain the low FeO values measured for the cryptomare deposits, and (5) the low Th values (Fig. 8). The low-Ti mare basalt modeled in this study matches most closely with the cryptomaria band centers (Fig. 9b), but other mare basalt spectra may also provide band centers consistent with the cryptomaria modeled in this study.

6. Conclusions

M^3 and LP data have been used to determine which ancient lunar rock type is most consistent with the observed mineralogical and compositional characteristics of mapped cryptomaria. The MGM was used to estimate the position of the 1 μm and 2 μm absorption features in the sampled M^3 cryptomare spectra. In addition, different M^3 optical period data sets have been compared to determine how the model-derived mineralogies vary due to spacecraft temperature. We find:

- (1) The model-derived 2 μm band position of M^3 spectra is estimated at shorter wavelengths than expected based on laboratory measurements of natural and synthetic pyroxenes. This shift in the 2 μm absorption band center is due partly to the continuum removal process and to the residual thermal effects in the M^3 .
- (2) The derived pyroxene mineralogies of cryptomaria are generally consistent with exposed mare basalts in the same local

- region (e.g., Australe, Smythii, South Pole–Aitken). In addition, in most cryptomaria there is little observable variation in the model-derived pyroxene mineralogy (Fig. 7).
- (3) There are a few cryptomare regions (e.g., Schiller–Schickard, West Humorum) with significant variation in the calculated pyroxene mineralogies, especially in the position of the 2 μm absorption band (Fig. 7). This observed variation cannot all be attributed to thermal effects because all of the collected cryptomare spectra contain residual thermal energy and neither Schiller–Schickard or West Humorum are associated with thermal anomalies on the surface; both of these cryptomaria are located at similar mid-latitudes away from the lunar poles and the equator. A geologic process associated with volcanism, magma evolution or magma source heterogeneities, is likely responsible for the observed mineralogic variations in cryptomaria and maria spectra.
- (4) The LP GRS measurements were measured over large areas, meaning these values represent an average of the ejecta of DHCs and the superposed feldspathic basin ejecta deposits. Therefore, the anomalously low values of FeO and Th that suggest Mg-rich lithologies (Fig. 8) can actually be explained by regolith mixing processes.
- (5) Of the ancient igneous rocks considered (low-Ti mare basalts, high-Ti mare basalts, Mg-suite rocks, dunite, high-Al mare basalts, KREEP basalts), only the mare basalts have absorption band centers and FeO and Th concentrations consistent with the sampled cryptomaria spectra and are expected to have been erupted as areally extensive volcanic deposits.

Acknowledgments

We thank S. Besse and H. Clenet for their constructive reviews of this manuscript. This research was supported by the NASA Solar System Exploration Research Virtual Institute (SSERVI) grant for Evolution and Environment of Exploration Destinations under cooperative agreement number NNA14AB01A at Brown University.

Appendix A. Supporting information

Supplementary data associated with this article can be found in the online version at <http://dx.doi.org/10.1016/j.pss.2014.11.027>.

References

- Adams, J.B., 1974. Visible and near-infrared diffuse reflectance spectra of pyroxenes as applied to remote sensing of solid objects in the solar system. *J. Geophys. Res.* 79, 4829–4836.
- Antonenko, I., 1999. Global estimates of cryptomare deposits: implications for lunar volcanism. *Lunar Planet. Sci. Conf.* 30 (abstract 1703).
- Antonenko, I., Head, J.W., Mustard, J.F., Hawke, B.R., 1995. Criteria for the detection of lunar cryptomaria. *Earth Moon Planets* 69, 141–172.
- Bandfield, J.L., Hayne, P.O., Paige, D.A., 2014. What is the surface temperature of the Moon. *Lunar Planet. Sci. Conf.* 45 (abstract 1519).
- Bell, J.F., Hawke, B.R., 1984. Lunar dark-haloed impact craters: origin and implications for early mare volcanism. *J. Geophys. Res.* 89, 6899–6910.
- Besse, S., Yokota, Y., Boardman, J., Green, R., Haruyama, J., Isaacson, P., Mall, U., Matsunaga, T., Ohtake, M., Pieters, C., Staid, M., Sunshine, J., Yamamoto, S., 2013. One moon, many measurements 2: photometric corrections. *Icarus* 226, 127–139. <http://dx.doi.org/10.1016/j.icarus.2013.05.009>.
- Blewett, D.T., Hawke, B.R., Lucey, P.G., Taylor, G.J., 1995. Remote sensing and geological studies of the Schiller–Schickard region of the Moon. *J. Geophys. Res.* 100, 16959–16977.
- Boardman, J.B., Pieters, C.M., Green, R.O., Lundein, S.R., Varanasi, P., Nettles, J., Petro, N., Isaacson, P., Besse, S., Taylor, L.A., 2011. Measuring moonlight: an overview of the spatial properties, lunar coverage, selenolocation, and related Level 1B products of the Moon Mineralogy Mapper. *J. Geophys. Res.* 116. <http://dx.doi.org/10.1029/2010JE003730>.
- Burns, R.G., 1970. Crystal field spectra and evidence of cation ordering in olivine minerals. *Am. Mineral.* 55, 1608–1632.
- Cadogan, P.H., 1974. Oldest and largest lunar basin? *Nature* 250, 315–316.
- Campbell, B.A., Hawke, B.R., 2005. Radar mapping of lunar cryptomaria east of Orientale basin. *J. Geophys. Res.* 110, E09002. <http://dx.doi.org/10.1029/2005JE002425>.
- Carli, C., Ciarniello, M., Capaccioni, F., Serventi, G., Sgavetti, M., 2014. Spectral variability of plagioclase–mafic mixtures (2): investigation of the optical constant and retrieved mineral abundance dependence on particle size distribution. *Icarus* 235, 207–219. <http://dx.doi.org/10.1016/j.icarus.2014.03.022>.
- Cheek, L.C., Donaldson Hanna, K.L., Pieters, C.M., Head, J.W., Whitten, J.L., 2013. The distribution and purity of anorthosites across the Orientale basin: new perspectives from Moon Mineralogy Mapper data. *J. Geophys. Res.* 118, 1–16. <http://dx.doi.org/10.1002/jgre.20126>.
- Clark, R.N., Pieters, C.M., Green, R.O., Boardman, J.W., Petro, N.E., 2011. Thermal removal from near-infrared imaging spectroscopy data of the Moon. *J. Geophys. Res.* 116, E00G16. <http://dx.doi.org/10.1029/2010JE003751>.
- Clenet, H., Pinet, P., Daydou, Y., Heuripeau, F., Rosemburg, C., Baratoux, D., Chevrel, S., 2011. A new systematic approach using the Modified Gaussian Model: insight for the characterization of chemical composition of olivines, pyroxenes and olivine–pyroxene mixtures. *Icarus* 213, 404–422. <http://dx.doi.org/10.1016/j.icarus.2011.03.002>.
- Cloutis, E.A., Gaffey, M.J., 1991. Pyroxene spectroscopy revisited: spectral-compositional correlations and relationship to geochemistry. *J. Geophys. Res.* 96, 22809–22826.
- Conel, J.E., Nash, D.B., 1970. Spectral reflectance and albedo of Apollo 11 lunar samples: effects of irradiation and vitrification and comparison with telescopic observation. *Proc. Lunar Sci. Conf.* 11, 2013–2023.
- Gault, D.E., Hörz, F., Brownlee, D.E., Hartung, J.B., 1974. Mixing of the lunar regolith. *Proc. Lunar Sci. Conf.* 5, 2365–2386.
- Green, R.O., Pieters, C., Mouroulis, P., Eastwood, M., Boardman, J., Glavich, T., Isaacson, P., Annadurai, M., Besse, S., Barr, D., Buratti, B., Cate, D., Chatterjee, A., Clark, R., Cheek, L., Combe, J., Dhingra, D., Essandoh, V., Geier, S., Goswami, J.N., Green, R., Haemmerle, V., Head, J., Hovland, L., Hyman, S., Klima, R., Koch, T., Kramer, G., Kumar, A.S.K., Lee, K., Lundein, S., Malaret, E., McCord, T., McLaughlin, S., Mustard, J., Nettles, J., Petro, N., Plourde, K., Racho, C., Rodriguez, J., Runyon, C., Sellar, G., Smith, C., Sobel, H., Staid, M., Sunshine, J., Taylor, L., Thaisen, K., Tompkins, S., Tseng, H., Vane, G., Varanasi, P., White, M., Wilson, D., 2011. The Moon Mineralogy Mapper (M^3) imaging spectrometer for lunar science: instrument description, calibration, on-orbit measurements, science data calibration and on-orbit validation. *J. Geophys. Res. Planets* 116, E00G19. <http://dx.doi.org/10.1029/2011JE003797>.
- Giguere, T.A., Hawke, B.R., Blewett, D.T., Bussey, D.B.J., Lucey, P.G., Smith, G.A., Spudis, P.D., Taylor, G.J., 2003. Remote sensing studies of the Lomonosov–Fleming region of the Moon. *J. Geophys. Res.* 108, 5118. <http://dx.doi.org/10.1029/2003JE002069>.
- Haskin, L.A., 1998. The Imbrium impact event and the thorium distribution at the lunar highlands surface. *J. Geophys. Res.* 103, 1679–1689.
- Hawke, B.R., Head, J.W., 1977. Pre-Imbrium history of the Fra Mauro region and Apollo 14 sample provenance. *Proc. Lunar Planet. Sci. Conf.* 8, 2741–2761.
- Hawke, B.R., Spudis, P.D., 1980. Geochemical anomalies on the eastern limb and farside of the moon. *Proc. Conf. Lunar Highl. Crust.* 467–481.
- Hawke, B.R., Bell, J.F., 1981. Remote sensing studies of lunar dark-halo impact craters: preliminary results and implications for early volcanism. *Proc. Lunar Planet. Sci. Conf.* 12B, 665–678.
- Hawke, B.R., Peterson, C.A., Lucey, P.G., Taylor, G.J., Blewett, D.T., Campbell, B.A., Coombs, C.R., Spudis, P.D., 1993. Remote sensing studies of the terrain northwest of Humorum Basin. *Geophys. Res. Lett.* 20, 419–422.
- Hawke, B.R., Giguere, T.A., Blewett, D.T., Lucey, P.G., Smith, G.A., Taylor, G.J., Spudis, P.D., 2002. Igneous activity in the southern highlands of the Moon. *J. Geophys. Res.* 107, 5122. <http://dx.doi.org/10.1029/2000JE001494>.
- Hawke, B.R., Blewett, D.T., Bussey, D.B.J., Giguere, T.A., Lawrence, D.J., Lucey, P.G., Smith, G.A., Spudis, P.D., Taylor, G.J., 2003. Geochemical anomalies in the lunar highlands. *Lunar Planet. Sci. Conf.* 34 (abstract 1198).
- Hawke, B.R., Gillis, J.J., Giguere, T.A., Blewett, D.T., Lawrence, D.J., Lucey, P.G., Smith, G.A., Spudis, P.D., Taylor, G.J., 2005. Remote sensing and geologic setting of the Balmer–Kapteyn region of the Moon. *J. Geophys. Res.* 110, E06004. <http://dx.doi.org/10.1029/2004JE002383>.
- Hawke, B.R., Giguere, T.A., Gaddis, L.R., Gustafson, J.O., Lawrence, D.J., Stopar, J.D., Peterson, C.A., Bell III, J.F., Robinson, M.S., The LROC Science Team, 2013. Cryptomare and pyroclastic deposits on the northern east side of the Moon. *Lunar Planet. Sci. Conf.* 44 (abstract 1883).
- Head, J.W., Wilson, L., 1979. Alphonsus-type dark-halo craters: morphology, morphometry and eruption condition. *Proc. Lunar Planet. Sci. Conf.* 10, 2861–2897.
- Head, J.W., Wilson, L., 1992. Lunar mare volcanism: stratigraphy, eruption conditions, and the evolution of secondary crusts. *Geochim. Cosmochim. Acta* 56, 2155–2175. [http://dx.doi.org/10.1016/0016-7037\(92\)90183-J](http://dx.doi.org/10.1016/0016-7037(92)90183-J).
- Head, J.W., Murchie, S., Mustard, J.F., Pieters, C.M., Neukum, G., McEwen, A., Greeley, R., Nagel, E., Bleton, M.J.S., 1993. Lunar impact basins: new data for the western limb and far side (Orientale and South Pole–Aitken basins) from the first Galileo flyby. *J. Geophys. Res.* 98, 17149–17181.
- Hess, P.C., Parmentier, E.M., 1995. A model for the thermal and chemical evolution of the Moon's interior: implications for the onset of mare volcanism. *Earth Planet. Sci. Lett.* 134, 501–514.

- Hiesinger, H., Head, J.W., Wolf, U., Jaumann, R., Neukum, G., 2011. Ages and stratigraphy of lunar mare basalts: a synthesis. *Geol. Soc. Am. Spec. Pap.* 477, 1–51.
- Hiroi, T., Pieters, C.M., Noble, S.K., 2000. Improved scheme of Modified Gaussian deconvolution for reflectance spectra of lunar soils. *Lunar Planet. Sci. Conf.* 31 (abstract 1548).
- Isaacson, P.J., Basu Sarbadhikari, A., Pieters, C.M., Klima, R.L., Hiroi, T., Liu, Y., Taylor, L.A., 2011a. The lunar rock and mineral characterization consortium: deconstruction and integrated mineralogical, petrologic, and spectroscopic analyses of mare basalts. *Meteorit. Planet. Sci.* 46, 228–251. <http://dx.doi.org/10.1111/j.1945-5100.2010.01148.x>.
- Isaacson, P.J., Pieters, C.M., Besse, S., Clark, R.N., Head, J.W., Klima, R.L., Mustard, J.F., Petro, N.E., Staid, M.I., Sunshine, J.M., Taylor, L.A., Thaisen, K.G., Tompkins, S., 2011b. Remote compositional analysis of lunar olivine-rich lithologies with Moon Mineralogy Mapper (M^3) spectra. *J. Geophys. Res.* 116, E00G11. <http://dx.doi.org/10.1029/2010JE003731>.
- Isaacson, P.J., Petro, N.E., Pieters, C.M., Besse, S., Boardman, J.W., Clark, R.N., Green, R.O., Lundeen, S., Malaret, E., McLaughlin, S., Sunshine, J.M., Taylor, L.A., 2013. Development, importance, and effect of a ground truth correction for Moon Mineralogy Mapper reflectance data set. *J. Geophys. Res. Planets* 118, 369–381. <http://dx.doi.org/10.1002/jgre.20048>.
- Jolliff, B.L., Gillis, J.J., Haskin, L.A., Korotev, R.L., Wieczorek, M.A., 2000. Major lunar crustal terranes: surface expressions and crust–mantle origins. *J. Geophys. Res.* 105, 4197–4216.
- Kanner, L.C., Mustard, J.F., Gendrin, A., 2007. Assessing the limits of the Modified Gaussian Model for remote spectroscopic studies of pyroxenes on Mars. *Icarus* 187, 442–456.
- Klima, R.L., Pieters, C.M., Dyar, M.D., 2007. Spectroscopy of synthetic Mg–Fe pyroxenes I: spin-allowed and spin-forbidden crystal field bands in the visible and near-infrared. *Meteorit. Planet. Sci.* 42, 235–253.
- Klima, R.L., Pieters, C.M., Dyar, M.D., 2008. Characterization of the $1.2\text{ }\mu\text{m}$ M1 pyroxene band: extracting cooling history from near-IR spectra of pyroxenes and pyroxene-dominated rocks. *Meteorit. Planet. Sci.* 43, 1591–1604.
- Klima, R.L., Dyar, M.D., Pieters, C.M., 2011. Near-infrared spectra of clinopyroxenes: effects of calcium content and crystal structure. *Meteorit. Planet. Sci.* 46, 379–395. <http://dx.doi.org/10.1111/j.1945-5100.2010.01158.x>.
- Korotev, R.L., 1998. Concentrations of radioactive elements in lunar materials. *J. Geophys. Res.* 103, 1691–1701.
- Lawrence, D.J., Feldman, W.C., Barraclough, B.L., Binder, A.B., Elphic, R.C., Maurice, S., Thomsen, D.R., 1998. Global elemental maps of the Moon: the Lunar Prospector gamma-ray spectrometer. *Science* 281, 1484–1489. <http://dx.doi.org/10.1126/science.281.5382.1484>.
- Lawrence, D.J., Feldman, W.C., Elphic, R.C., Little, R.C., Prettyman, T.H., Maurice, S., Lucey, P.g., Binder, A.B., 2002. Iron abundances on the lunar surface as measured by the gamma-ray and neutron spectrometers. *J. Geophys. Res.*, 107. <http://dx.doi.org/10.1029/2001JE001530>.
- Lawrence, S.J., Hawke, B.R., Gillis-Davis, J.J., Taylor, G.J., Lawrence, D.J., Cahill, J.T., Hagerty, J.J., Lucey, P.G., Smith, G.A., Keil, K., 2008. Composition and origin of the Dewar geochemical anomaly. *J. Geophys. Res.* 113, E02001. <http://dx.doi.org/10.1029/2007JE002904>.
- Li, L., Mustard, J.F., 2000. Compositional gradients across mare–highlands contacts: importance and geological implication of lateral transport. *J. Geophys. Res.* 105, 20431–20450.
- Lucey, P.G., 1998. Model near-infrared optical constants of olivine and pyroxene as a function of iron content. *J. Geophys. Res.* 103, 1703–1713. <http://dx.doi.org/10.1029/97JE03145>.
- Lucey, P.G., Taylor, G.J., Malaret, E., 1995. Abundance and distribution of iron on the Moon. *Science* 268, 1150–1153.
- Lucey, P., Korotev, R.L., Gillis, J.J., Taylor, L.A., Lawrence, D., Campbell, B.A., Elphic, R., Feldman, W., Hood, L.L., Hunten, D., Mendillo, M., Noble, S., Papike, J.J., Reedy, R.C., Lawson, S., Prettyman, T., Gasnault, O., Maurice, S., 2006. Understanding the lunar surface and space–Moon interactions. *Rev. Mineral. Geochim.* 60, 83–219. <http://dx.doi.org/10.2138/rmg.2006.60.2>.
- Maxwell, T.A., Andre, C.G., 1981. The Balmer basin: regional geology and geochemistry of an ancient lunar impact basin. *Proc. Lunar Planet. Sci. Conf.* 12, 715–725.
- McCord, T.B., Adams, J.B., 1973. Progress in remote optical analysis of lunar surface composition. *The Moon* 7, 453–474.
- McCord, T.B., Taylor, L.A., Combe, J.-P., Kramer, G., Pieters, C.M., Sunshine, J.M., Clark, R.N., 2011. Sources and physical processes responsible for OH/H₂O in the lunar soil as revealed by the Moon Mineralogy Mapper (M^3). *J. Geophys. Res.* 116, E00G05. <http://dx.doi.org/10.1029/2010JE003711>.
- McEwen, A.S., Moore, J.M., Shoemaker, E.M., 1997. The Phanerozoic impact cratering rate: evidence from the farside of the Moon. *J. Geophys. Res.* 102, 9231–9242.
- Melosh, H.J., 1989. Impact Cratering: A Geologic Process. Oxford University Press, Oxford, UK p. 245.
- Mustard, J.F., Head, J.W., 1996. Buried stratigraphic relationships along the southwestern shores of Oceanus Procellarum: implications for early lunar volcanism. *J. Geophys. Res.* 101 (E02001), 18913–18925.
- Noble, S.K., Pieters, C.M., Hiroi, T., Taylor, L.A., 2006. Using the Modified Gaussian Model to extract quantitative data from lunar soils. *J. Geophys. Res.* 111, E11009. <http://dx.doi.org/10.1029/2006JE002721>.
- Nyquist, L.E., Shih, C.-Y., 1992. The isotopic record of lunar volcanism. *Geochim. Cosmochim. Acta* 56, 2213–2234.
- Nyquist, L.E., Bansal, B.M., Wiesmann, H., 1975. Rb-Sr ages and initial $^{87}\text{Sr}/^{86}\text{Sr}$ for Apollo 17 basalts and KREEP basalt 15386. *Proc. Lunar Planet. Sci. Conf.* 6, 1445–1465.
- Papanastassiou, D.A., Wasserburg, G.J., 1976. Rb-Sr age of troctolite 76535. *Proc. Lunar Planet. Sci. Conf.* 7, 2035–2054.
- Pieters, C.M., 1982. Copernicus crater central peak: Lunar mountain of unique composition. *Science* 215, 59–61.
- Pieters, C.M., 1983. Strength of mineral absorption features in the transmitted component of near-infrared reflected light: first results from RELAB. *J. Geophys. Res.* 88, 9534–9544. <http://dx.doi.org/10.1029/JB088iB11p09534>.
- Pieters, C.M., Rode, O., Basu, A., 1993. Optical effects of space weathering: the role of the finest fraction. *J. Geophys. Res.* 98, 20817–20824.
- Pieters, C.M., Tompkins, S., 1999. Tsiolovsky crater: a window into crustal processes on the lunar farside. *J. Geophys. Res.* 104, 21935–21949.
- Pieters, C.M., Goswami, J.N., Clark, R.N., Annadurai, M., Boardman, J., Buratti, B., Combe, J.-P., Dyer, M.D., Green, R., Head, J.W., Hibbits, C., Hicks, M., Isaacson, P., Klima, R., Kramer, G., Kumar, S., Livo, E., Lundeen, S., Malaret, E., McCord, T., Mustard, J., Nettles, J., Petro, N., Runyon, C., Staid, M., Sunshine, J., Taylor, L.A., Tompkins, S., Varanasi, P., 2009. Character and spatial distribution of OH/H₂O on the surface of the Moon as seen by M^3 on Chandrayaan-1. *Science* 326, 568–572. <http://dx.doi.org/10.1126/science.1178658>.
- Prettyman, T.H., 2012. Lunar Prospector GRS Elemental Abundance, LP-L-GRS-5-ELEM-ABUNDANCE-V1.0, NASA Planetary Data System.
- Prettyman, T.H., Hagerty, J.J., Elphic, R.C., Feldman, W.C., Lawrence, D.J., McKinney, G.W., Vaniman, D.T., 2006. Elemental composition of the lunar surface: analysis of gamma-ray spectroscopy data from Lunar Prospector. *J. Geophys. Res.* 111, E12007. <http://dx.doi.org/10.1029/2005JE002656>.
- Prissel, T.C., Parman, S.W., Head, J.W., Wilson, L., 2013. Mg-suite plutons: implications for mantle-derived primitive magma source depths on the Moon. *Lunar Planet. Sci. Conf.* 44 (abstract 3041).
- Ryder, G., 1987. Petrologic evidence for nonlinear cooling rates and a volcanic origin for Apollo 15 KREEP basalts. *J. Geophys. Res.* 92, E331–E339.
- Ryder, G., Spudis, P., 1980. Volcanic rocks in the lunar highlands. *Proc. Conf. Lunar Highl. Crust.* 353–375.
- Schultz, P.H., Spudis, P.D., 1979. Evidence for ancient mare volcanism. *Proc. Lunar Planet. Sci. Conf.* 10, 2899–2918.
- Schultz, P.H., Spudis, P.D., 1983. The beginning and end of lunar mare volcanism. *Nature* 302, 233–236.
- Shoemaker, E.M., Interpretation of lunar craters. In: Kopal Z., (Ed), Physics and Astronomy of the Moon, 1962, Academic, New York, 283–359.
- Shoemaker, E.M., Hait, M.H., Swann, G.A., Schleicher, D.L., Schaber, G.G., Sutton, R.L., Dahlem, D.H., Goddard, E.N., Waters, A.C., 1970. Origin of the lunar regolith at Tranquillity base. *Proc. Apollo 11 Lunar Sci. Conf.* 3, 2399–2412.
- Smith, J.V., Anderson, A.T., Newton, R.C., Olsen, E.J., Wyllie, P.J., Crewe, A.V., Isaacson, M.S., Johnson, D., 1970. Petrologic history of the moon inferred from petrography, mineralogy, and petrogenesis of Apollo 11 rocks. *Proc. Apollo 11 Lunar Sci. Conf.* 1, 897–925.
- Solomon, S.C., 1975. Mare volcanism and lunar crustal structure. *Proc. Lunar Planet. Sci. Conf.* 6, 1021–1042.
- Spera, F.J., 1992. Lunar magma transport phenomena. *Geochim. Cosmochim. Acta* 56, 2253–2265. [http://dx.doi.org/10.1016/0016-7037\(92\)90187-N](http://dx.doi.org/10.1016/0016-7037(92)90187-N).
- Spudis, P.D., 1978. Composition and origin of the Apennine Bench formation. *Proc. Lunar Planet. Sci. Conf.* 9, 3379–3394.
- Stöffler, D., Ryder, G., Ivanov, B.A., Artemieva, N.A., Cintala, M.J., Grieve, R.A.F., 2006. Cratering history and lunar chronology. *Rev. Min. Geochem.* 60, 519–596.
- Sunshine, J.M., Pieters, C.M., 1990. Deconvolution of mineral absorption bands: an improved approach. *J. Geophys. Res.* 95, 6955–6966.
- Sunshine, J.M., Pieters, C.M., 1993. Estimating model abundances from the spectra of natural and laboratory pyroxene mixtures using the Modified Gaussian Model. *J. Geophys. Res.* 98, 9075–9087.
- Taylor, L.A., Shervais, J.W., Hunter, R.H., Shih, C.-Y., Bansal, B.M., Wooden, J., Nyquist, L.E., Laul, L.C., 1983. Pre-4.2 AE mare–basalt volcanism in the lunar highlands. *Earth Planet. Sci. Lett.* 66, 33–47.
- Terada, K., Anand, M., Sokol, A.K., Bischoff, A., Sano, Y., 2007. Cryptomare magmatism 4.35 Gyr ago recorded in lunar meteorite Kalahari 009. *Nature* 450, 849–852. <http://dx.doi.org/10.1038/nature06356>.
- Tompkins, S., Pieters, C.M., 1999. Mineralogy of the lunar crust: results from Clementine. *Meteorit. Planet. Sci.* 34, 25–41.
- Ullrich, G.W., Roddy, D.J., Simmons, G., 1977. Numerical simulation of a 20-ton TNT detonation on the Earth's surface. In: Roddy, D.J., Pepin, R.O., Merrill, R.B. (Eds.), Impact and Explosion Cratering. Pergamon Press, New York, p. 959.
- Warren, P.H., Wasson, J.T., 1977. Pristine nonmare rocks and the nature of the lunar crust. *Proc. Lunar Planet. Sci. Conf.* 8, 2215–2235.
- Whitten, J.L., Head, J.W., 2015. Lunar cryptomaria: physical characteristics, distribution, and implications for ancient volcanism. *Icarus* 247, 150–171. <http://dx.doi.org/10.1016/j.icarus.2014.09.031>.
- Wieczorek, M.A., Jolliff, B.L., Khan, A., Pritchard, M.E., Weiss, B.P., Williams, J.G., Hood, L.L., Righter, K., Neal, C.R., Shearer, C.K., McCallum, I.S., Tompkins, S., Hawke, B.R., Peterson, C., Gillis, J.J., Bussey, B., 2006. The constitution and structure of the lunar interior. *Rev. Mineral. Geochem.* 60, 221–364. <http://dx.doi.org/10.2138/rmg.2006.60.3>.
- Wieczorek, M.A., Neumann, G.A., Nimmo, F., Kiefer, W.S., Talor, G.J., Melosh, H.J., Phillips, R.J., Solomon, S.C., Andrews-Hanna, J.C., Asmar, S.W., Konopliv, A.S., Lemoine, F.G., Smith, D.E., Watkins, M.M., Williams, J.G., Zuber, M.T., 2013. The crust of the Moon as seen by GRAIL. *Science* 339, 671–675. <http://dx.doi.org/10.1126/science.1231530>.

- Wilhelms, D.E., 1987. The geologic history of the Moon. US Geological Survey Professional Paper 1348.
- Wilhelms, D.E., McCauley, J.F., 1971. Geologic map of the near side of the Moon. US Geo. Survey Map I-703, Reston, VA.
- Wood, J.A., Dickey Jr., J.S., Marvin, U.B., Powell, B.N., 1970. Lunar anorthosites and a geophysical model of the moon. Proc. Apollo 11 Lunar Sci. Conf. 1, 965–988.
- Yamamoto, S., Nakamura, R., Matsunaga, T., Ogawa, Y., Ishihara, Y., Morota, T., Hirata, N., Otake, M., Hiroi, T., Yokota, Y., Haruyama, J., 2010. Possible mantle origin of olivine around lunar impact basins detected by SELENE. Nat. Geosci. 3, 533–536. <http://dx.doi.org/10.1038/NGEO897>.